Ben-Gurion University of the Negev
Faculty of Engineering Sciences
School of Electrical and Computer Engineering
Electro-optics and Photonics Engineering Department

Integrated Photonics in the Sub-wavelength Regime

by

Yakov Greenberg

A thesis submitted in partial fulfillment of the requirements for the degree of Master of Science

Under the supervision of

Dr. Alina Karabchevsky

September 2019

Ben-Gurion University of the Negev
Faculty of Engineering Sciences
School of Electrical and Computer Engineering
Electro-optics and Photonics Engineering Department

Integrated Photonics in the Sub-wavelength Regime

by

Yakov Greenberg

A thesis submitted in partial fulfillment of the requirements for the degree of Master of Science

Under the supervision of

Dr. Alina Karabchevsky

Yakov Greenberg | 07/01/2020
Author | *Date*

Karabchevsky | 08/01/2020
Supervisor | *Date*

08-1-2020
Chairman of Graduate Studies Committee | *Date*

September 2019

Abstract

The macroscopic behavior of materials in an electromagnetic field is determined by quantities which arise from their microscopic properties, attributed to their atomic structure. In analogy to the atoms in the naturally occurring conventional materials, metamaterials, with their unique properties which arise from subwavelength structuring, are capable of manipulating electromagnetic waves to achieve benefits that go beyond what is possible with conventional materials. Metamaterials have drawn broad interest and have led to possible utilization in many electromagnetic applications from the microwave to optical regime, and especially for guided-wave devices.

In this work, we explore how metamaterials can be used to enhance the performance of integrated photonic devices and increase their functionalities. By employing the concepts of transformation optics, we demonstrate evanescent field cloaking on a waveguide, where the fields propagating in a waveguide are manipulated and controlled in a way that the scattered fields of an object located on a waveguide do not interact with the evanescent field, resulting in its invisibility.

We explore the discrete nature of waveguide modes and the effective medium concept to achieve a simple, yet compact and efficient waveguide mode conversion devices with more than 90% efficiency. The conversion is realized using dielectric metasurfaces engraved in the silicon waveguide, and the technique can be generalized to realize arbitrary mode conversions.

We develop a surface plasmon resonance sensor with 50% sensitivity enhancement compared to conventional configuration as result of an optimized multilayer film structure. Simultaneous wavelength and angular interrogations are conducted to characterize the sensor performance.

We demonstrate that highly transmissive facets can be formed on silicon waveguides by subwavelength gradient structures and achieve over 98% transmittance. The optimal structure is obtained by extensive numerical simulations.

For each project, we present the fundamental concepts and the analysis required for the comprehension of light propagation in subwavelength optical structures. The theoretical derivations as well as numerical and experimental observations are summarized and analyzed in this thesis.

Contents

List of Figures

List of Tables

Abbreviations

Notation	Description
AR	Anti-Reflection
CFA	Complex Field Amplitude
CMT	Coupled Mode Theory
CPW	Composite Plasmonic Waveguide
EM	Electromagnetic
EMT	Effective Medium Theory
FDTD	Finite Difference Time Domain
FEM	Finite Element Method
GRIN	Graded Index
IDE	Integrated Design Environment
LD	Lorentz-Drude (Material Dispersion Model)
LSPR	Localized Surface Plasmon Resonance
MDM	Mode Division Multiplexing
NGWSPR	Nearly Guided Wave Surface Plasmon Resonance
NIR	Near Infrared
PDE	Partial Differential Equation
QCTO	Quasi-Conformal Transformation Optics
RI	Refractive Index
SOI	Silicon-on-Insulator
SP	Surface Plasmon
SPP	Surface Plasmon Polariton
SPR	Surface Plasmon Resonance
TE	Transverse Electric
TIR	Total Internal Reflection
TM	Transverse Magnetic
TO	Transformation Optics
VIS	Visible (spectral range)
WDM	Wavelength Division Multiplexing

Symbols and Constants

Symbol	Description	Value	Units
N	Complex Refractive Index	-	rad
$\hbar$	Reduced Planck Constant	$1.054571800 \times 10^{-34}$	$\mathrm{J \cdot s}$
κ	Extinction Coefficient	-	-
ω	Angular Frequency	-	$\mathrm{rad \cdot s^{-1}}$
ω_p	Plasma Frequency	-	$\mathrm{rad \cdot s^{-1}}$
ε_r	Relative Permittivity	-	$\mathrm{F \cdot m^{-1}}$
c_0	Velocity of Light in Vacuum	299792458	$\mathrm{m \cdot s^{-1}}$
h	Planck's Constant	$6.62607004 \times 10^{-34}$	$\mathrm{J \cdot s}$
n	Refractive Index	-	-
Ag	Silver (Element Symbol)	-	-
Au	Gold (Element Symbol)	-	-
Si	Silicon (Element Symbol)	-	-
Si_3N_4	Silicon Nitrate (Chemical Formula)	-	-
SiO_2	Silicon Dioxide (Chemical Formula)	-	-

1 Introduction

The development of novel functional materials have always played an important role in the evolution of human civilization throughout the ages. Since light is omnipresent in our world, and its widespread application in nearly every area, controlling electromagnetic waves through engineered materials is of particular importance.

Traditionally, the materials for optical devices and applications were mainly made from transparent glasses, reflective metals and various optical thin films [1]. These bulk materials selectively refract and reflect light according to Snell's law, Fermat's principle, Fresnel's equations and Fresnel-Kirchhoff's diffraction formula [2]. The ever-growing interest in upgrading the performance of classical optical devices and overcoming the fundamental difficulties had to face several major challenges including surmounting the diffraction limit and other restrictions set by classical theories, and reducing the complexity and cost of optical systems.

In the last decades, the manufacturing scale of optical materials was expanded into dimensions smaller than the wavelength, and allowed exploiting the light scattered by subwavelength structures, where the light propagation can be tuned almost arbitrarily [3, 4]. In addition, full-vectorial electromagnetic computational algorithms have facilitated the rigorous designs of complex structures with multiscale characteristic dimensions [5].

At the nanoscale, subwavelength light-matter interaction is blended with classic and quantum effects in various functional materials such as noble metals [6, 7], semiconductors [8], phase-change materials [9, 10], and 2D materials [11, 12]. These so-called metamaterials [13] provide unprecedented opportunities to upgrade the performance of classic optical devices. Metamaterials are artificial materials with subwavelength features which act as miniature, anisotropic light scatterers. As a result, the phase, amplitude and polarization of light can be engineered to provide the desired optical response.

Here, we incorporate metamaterials into integrated photonic devices and explore how they can be used to enhance their performance, such as reducing waveguide facet reflection losses with anti-reflective structures, engineering the waveguide effective index to convert the propagating modes, and demonstrate phenomenon of evanescent field cloaking on a chip. We present the basic concepts of electromagnetic wave theory required for the comprehension of light propagation in subwavelength optical structures, investigate phenomena associated with the propagation and manipulation of light in dielectric waveguides and waveguides with plasmonic overlayer, and review the theory of guided wave optics. Additionally, we provide an overview of the general properties of surface plasmon polaritons and examine how their propagation can be manipulated. Finally, we present the outcomes of our work done in the fields of surface plasmon resonance sensors, evanescent field waveguide cloaking [14], waveguide facet anti-reflective structures, and waveguide mode conversion on silicon waveguides [15].

1.1 Motivation

Metamaterials have tremendous potential in many fields of science and technology. Nevertheless, the major scientific breakthroughs based on metamaterials, including invisibility cloaks [16, 17, 18], super lenses [19, 20], and negative refraction [21, 22, 23, 24] were demonstrated primarily in free-space optics. The recent developments in metamaterial science and nanotechnology have enabled the possibility of incorporating metamaterials into guided-wave optical devices [25, 26, 27, 28].

The main aim of this research activity is to address the issues associated with combining the technologies of guided-wave optical devices and metamaterials, and expanding the applications of integrated photonic devices. Our objectives include the design of a waveguide cloak by utilizing the light confinement in metallic structures, reducing coupling losses by engineering the facets of silicon waveguides, converting between waveguide modes using a compact and simple scheme, and increasing the sensitivity of surface plasmon resonance sensors through optimization of a multilayer thin film structure.

1.2 Theoretical Background

Grasping the fundamental properties of materials and their behavior in an electromagnetic field is essential for the development of metamaterials. Furthermore, waveguides and thin film structures are fundamental building blocks in integrated photonic devices and sensors. In this chapter, we introduce the basis of waveguides and surface plasmon polaritons (SPPs).

1.2.1 Surface Plasmon Polaritons

SPPs [29, 30, 31] are evanescent electromagnetic waves propagating along a metal-dielectric interface that are strongly coupled to coherent oscillations of free charges at the metal surface. SPPs are widely used for various applications [32] such as chemical and biological sensors [33], microscopy [34], and light sources [35].

In this work, we utilize the resonant behavior of SPPs and their ability to confine light in subwavelength scales [36] to increase the sensitivity of biological sensors and as means to localize light in plasmonic overlayers deposited on waveguides. The unique nature of SPPs and their interaction with light arises from the various optical properties of the materials.

1.2.1.1 Optical Constants and Properties

The optical properties of a material dictate the changes that light undergoes upon interacting with it and arise from its macroscopic and microscopic properties [37, 38]. The optical properties are associated with important optical constants, namely the relative permittivity ε_r, refractive index n and the extinction coefficient κ.

The precision of the various optical constants dictates the accuracy of the theoretical and numerical modeling of the investigated optical phenomena. The constants depend on the interaction between atoms and the applied electric fields. Therefore, choosing the appropriate material model is of very high importance.

Drude-Lorentz Model While the dispersion of light in simple transparent materials is usually determined by empirical methods [39], the optical constants of metals and semiconductors are modeled based on the harmonic oscillator model of the carriers in a material. The problem is treated as an electron-spring system connected to an infinite mass of the nucleus in an atom. The frequency dependent permittivity is obtained by taking in account the driving and the damping forces an electron experiences, and described by the sum of multiple resonant functions.

Both bound and free electrons contribute to the optical properties. The complex dielectric permittivity contains both the Drude component for the intraband effect and the Lorentz term for the interband transition in the form of the Lorentz-Drude (LD) model [40, 41]

$$\varepsilon(\omega) = 1 - \frac{\omega_p^2}{\omega^2 + j\omega\gamma_d} + \sum_{i=1}^{K} \frac{f_i \omega_i^2}{\omega_i^2 - \omega^2 - j\omega\gamma_i} \tag{1.1}$$

where ω is the angular frequency, and ω_p is the plasma frequency with damping constant γ_d. In the second term, K is the total number of oscillators with resonant frequency ω_j, strength f_j, and relaxation time $1/\gamma_j$. The relative permittivity is a complex function with real part ε_r' and imaginary part ε_r''.

The values of silver (Ag) and gold (Au) for the LD model are listed in Table 1.1 [42]. In this work, we use these noble metals for our plasmonic applications.

Table 1.1: Lorentz-Drude model parameter values for common metals used in plasmonic devices [42].

	f_0	γ_d	f_1	γ_1	ω_1	f_2	γ_2	ω_2	f_3	γ_3	ω_3	f_4	γ_4	ω_4	f_5	γ_5	ω_5
Ag	0.845	0.048	0.065	3.886	0.816	0.124	0.452	4.481	0.011	0.065	8.815	0.840	0.916	9.083	5.646	2.419	20.29
Au	0.760	0.053	0.024	0.241	0.415	0.010	0.345	0.830	0.071	0.870	2.969	0.601	2.494	4.304	4.384	2.214	13.32

The calculated dielectric permittivities of silver and gold are plotted as a function of wavelength in Fig. 1.1a. At optical frequencies, the magnitudes of the imaginary parts of the both dielectric permittivity and the refractive index are much greater than the real part.

We use the LD model in our calculations to enable us to take advantage of semiconductors and metals at optical frequencies and search for a possibility of an optical plasmon existence in that range.

Refractive Index and Extinction Coefficient The refractive index (RI) n of a material is the ratio of the velocity of light in vacuum c_0 to its velocity v in

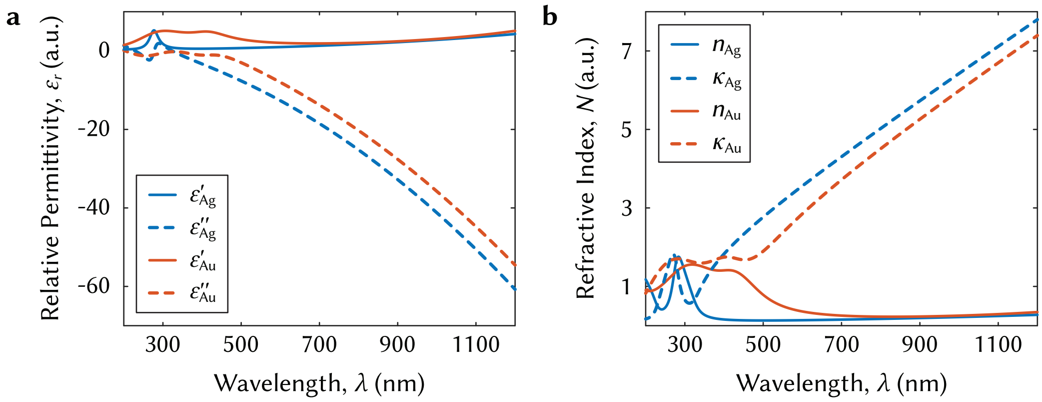

Figure 1.1 | Dielectric permittivity and the complex refractive index of common metals used in plasmonic devices. a, Dielectric permittivity of silver and gold. **b**, Complex refractive index of silver and gold. The imaginary parts are much greater than the real part at optical wavelengths.

the medium $n = c_0/v = \sqrt{\varepsilon_r \mu_r}$. An electromagnetic wave propagating through a lossy medium also experiences attenuation. In such materials, the RI is a complex function N, with real part n and imaginary part κ called the extinction coefficient. Since most naturally occurring materials are non-magnetic at optical frequencies, the relative permeability μ_r is assumed to be unity. Therefore, N is related to the complex relative permittivity by

$$N = n - i\kappa = \sqrt{\varepsilon_r} = \sqrt{\varepsilon'_r - \varepsilon''_r} \tag{1.2}$$

As seen from Fig. 1.1a, at wavelengths longer than the resonant wavelength, the imaginary part of the RI is incrementally greater than the corresponding real part, which is slightly larger than zero. This is an indication about the large losses associated with plasmons.

The best choice of material for plasmonic applications is one that has the lowest loss (and therefore the smallest dampening rate), and is stable in the environment in which it would be used. In addition to a low dampening rate, the chosen material has to support plasmons of the desired energy without inducing intraband transitions. Looking Table 1.1, one can see that silver has a lower dampening rate (γ_d) and is able to support plasmons that span the entire VIS-NIR spectrum due to the vicinity of the interband transition frequencies. Therefore, we choose silver as the metal in our surface plasmon resonance (SPR) sensor.

1.2.1.2 Dispersion Relation

The energy absorbed by metals from an incident electromagnetic (EM) field can cause free charges to oscillate in unison with the applied electric field. This collective electron oscillation excited at a metal-dielectric interface is known as surface plasmons (SPs).

Solving Maxwell's equations for the electromagnetic wave at the interface between a metal and dielectric half spaces under the appropriate boundary conditions provides the dispersion relation [41]

$$k_x = k_{\mathrm{SP}} = k_0 \sqrt{\frac{\varepsilon_d \varepsilon_m}{\varepsilon_d + \varepsilon_m}} \tag{1.3}$$

where k_{SP} is the frequency dependent SP wavevector parallel to the interface, $k_0 = \omega / c_0$ is the free-space wavevector, ε_d and ε_m are the permittivities of the dielectric and the metal, respectively.

The dispersion relation for a single metal-dielectric interface is schematically plotted in Fig. 1.2a. When taking the Drude component only into consideration (no damping), the wavevector k_x increases with the frequency ω. As it reaches the SP frequency $\omega_{\mathrm{SP}} = \omega_p / \sqrt{1 + \varepsilon_d}$, the mode demonstrates electrostatic character and transforms to SPs. On the other hand, when considering damping as in the LD model, which is the actual situation in a real metal because of the intraband and interband transitions of electrons, it bends backwards filling the region called plasmon bandgap [43], and connects to the Brewster mode [44].

The field perpendicular to the interface varies on a subwavelength scale and described in terms of evanescent waves (see Fig. 1.2b), reflecting the bound, non-radiative nature of SPs, and prevents power from propagating away from the surface. This confinement is described by the normal component of the wave vector

$$k_{z,i} = \sqrt{\varepsilon_i \left(\frac{\omega}{c_0} \right)^2 - k_{SP}^2} \tag{1.4}$$

where ε_i is the relative permittivity ε_m for the metal and ε_d for the dielectric medium. The SP exponentially decays into the surrounding media as it propagates along the surface. The penetration depths are given by substituting Eq. (1.4) into Eq. (1.3) and taking the real parts of the complex permittivity

$$\delta_i = \frac{\lambda}{2\pi}\sqrt{\frac{\varepsilon_m + \varepsilon_d}{{\varepsilon_i}^2}} \tag{1.5}$$

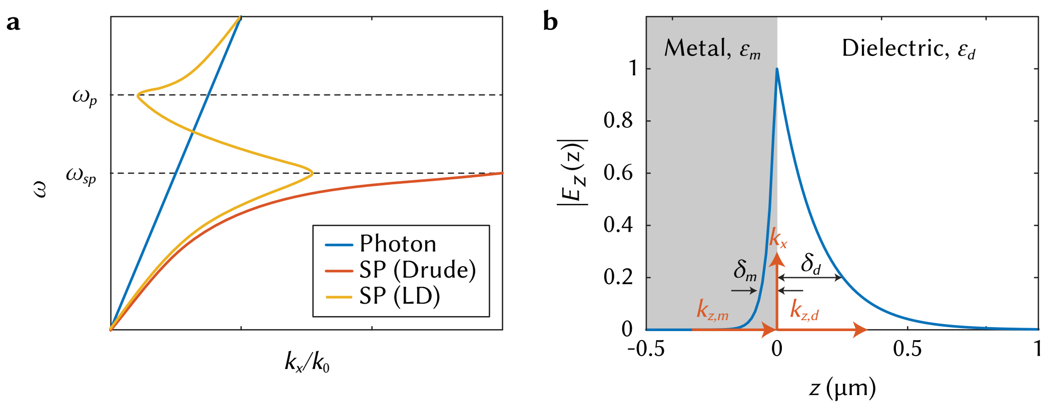

Figure 1.2 | Dispersion relation and evanescent decay of SPs at a single metal-dielectric interface. **a**, The dispersion curve for a SP. At low wavevectors, the SP curve approaches the propagating free-space curve. **b**, The field in the perpendicular direction is evanescent and exponentially decays into the surrounding materials.

1.2.1.3 Coupling, Propagation, and Excitation of SPPs

The dispersion curve of the SP in Fig. 1.2b stays to the right of the vacuum curve $\omega = c_0 k_0$. The momentum of the SP wavevector $\hbar k_{\mathrm{SP}}$, where $\hbar{=}h/2\pi$ is the reduced Planck constant, is greater than that of a free-space photon of the same frequency $\hbar k_0$ and in order to couple light and SPs together, their momenta must be matched, resulting in SPPs. Such SPPs cannot be excited by an impinging plane wave on the interface. Yet, the missing momentum can be obtained with the help of frustrated TIR, which increases k_{SP} beyond its vacuum value resulting in SPR.

Propagation of Surface Plasmons In contrary to a single metal-dielectric interface in Fig. 1.2b, a multilayer system consisting of alternating conducting and dielectric films can sustain bound SPPs on each single interface. When the separation between the adjacent interfaces is comparable to or smaller than the evanescent decay length of the interface mode, interactions between SPPs give rise to coupled modes.

The basic geometry supporting bound SPP modes is shown in Fig. 1.3a. In the so called dielectric-metal-dielectric (DMD) configuration, the system is composed of a thin metal film with thickness d and permittivity ε_m sandwiched between two dielectrics with permittivities ε_{d1} and ε_{d2}, respectively. The solution of wave equation for this structure must satisfy

$$k_i^2 = k_x^2 - k_0^2 \varepsilon_i \tag{1.6}$$

where k_i and ε_i are the wavevectors and dielectric constants in each region, and k_x is the wavevector in the direction of propagation. Thus, solving Maxwell's equation under the appropriate boundary conditions provides the dispersion relation

$$e^{-4k_1 d} = \left(\frac{k_1/\varepsilon_1 + k_2/\varepsilon_2}{k_1/\varepsilon_1 - k_2/\varepsilon_2}\right)\left(\frac{k_1/\varepsilon_1 + k_3/\varepsilon_3}{k_1/\varepsilon_1 - k_3/\varepsilon_3}\right) \tag{1.7}$$

Substituting Eq. (1.6) into Eq. (1.7) and solving for k_x provides two distinct solutions of the supported odd and even modes. Consider a symmetric DMD configuration of a silver film ($n_{\mathrm{Ag}} = 0.056440 + 4.2698i$ [45]) with thickness $d = 20$ nm sandwiched between two half spaces of crown glass ($n_{\mathrm{BK7}} = 1.5151$). The normalized components of the electric field perpendicular to the interface $E_z(z)$ of the bound odd and even modes at the wavelength $\lambda = 632.8$ nm are plotted in Fig. 1.3a.

The calculated propagation constants of the modes as a function of the silver layer thickness are plotted in Fig. 1.3b. Odd modes have the interesting property that upon decreasing metal film thickness, the confinement of the coupled SPP to the metal film decreases as the mode evolves into a plane wave supported by the homogeneous dielectric environment. The even modes exhibit the opposite behavior, their confinement to the metal increases with decreasing metal film thickness, resulting in a reduction in propagation length.

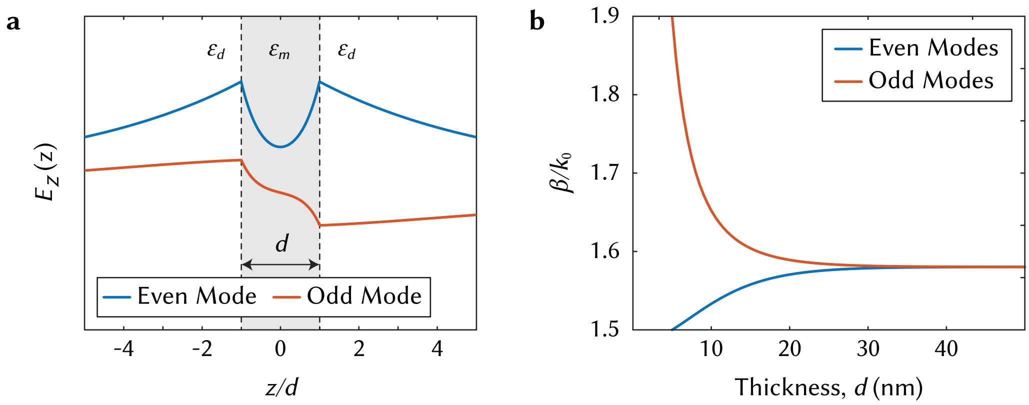

Figure 1.3 | Geometry and eigenmodes of a symmetric DMD system. **a**, Geometry of a symmetric DMD system consisting of a thin silver layer sandwiched between two infinite dielectric half spaces with the calculated normalized odd and even eigenmodes. **b**, Propagation constants of the odd and even modes as a function of layer thickness.

It will be shown later that these modes can be coupled with guided modes supported by dielectric waveguides by matching their corresponding propagation constants. Waveguides incorporating SPPs can support propagation mode tightly bounded to the metallic surfaces and confine the guiding wave in deep subwavelength scale. This feature is the principle behind using plasmonics in subwavelength integrated optical devices.

Surface Plasmon Resonance If a TM polarized plane wave is incident upon a metal-dielectric interface at an angle that is greater than the angle of TIR, then the corresponding wavenumber will be greater than its vacuum value and it could excite a plasmon wave along the interface. In the so-called Kretschmann-Raether (KR) configuration shown in Fig. 1.4a, a thin metal film of subwavelength scale with RI n and thickness d is sandwiched between a prism and air with RIs n_a and n_b, respectively. The TIR angle is $\theta_c = \arcsin\left(n_b/n_a\right)$, and the angle of incidence from the prism side is assumed to be $\theta \geq \theta_c$ so that

$$k_x = k_0 n_a \sin\theta \geq k_0 n_b \tag{1.8}$$

Because of Snell's law, the k_x component of the wavevector along the interface is preserved across the media. If there is a SP wave on the metal-air interface, then it will be characterized by the specific values given by Eq. (1.3) and Eq. (1.4). If the incidence angle θ is such that k_x is near the real part of k_{SP} given by Eq. (1.3), then a resonance takes place exciting the surface plasmon wave. This method of providing the missing momentum is referred to as the attenuated total reflection (ATR) method.

The reflection response measured at the prism side experiences a sharp drop at the resonant angle θ_{SP} given by

$$\theta_{\text{SP}} = \arcsin\left[\frac{1}{n_a}\sqrt{\frac{n_b^2 n^2}{n_b^2 + n^2}}\right] \tag{1.9}$$

The corresponding TM reflection response of the structure is given by

$$R = \left|\frac{r_a + r_b e^{-2ik_z d}}{1 + r_b e^{-2ik_z d}}\right|^2 \tag{1.10}$$

where d is the layer thickness, r_a and r_b denote the TM reflection coefficients at each interface given by

$$r_a = \frac{k_z n_a^2 - k_{za} n^2}{k_z n_a^2 + k_{za} n^2}\,, \qquad r_b = \frac{k_{zb} n^2 - k_z n_b^2}{k_{zb} n^2 + k_z n_b^2} \tag{1.11}$$

Fig. 1.4b shows the reflection response versus angle θ for a crown glass prism coated with a silver film with thickness $d = 40$ nm and air on the other side at wavelength $\lambda = 632.8$ nm. At the resonance angle, photons couple with the free electrons in the metal, and as a result, the reflection response measured at the prism side experiences sharp drop. Both the critical angle θ_c and the SPR angle θ_{sp} are indicated on the graph as dashed lines in Fig. 1.4b.

SPR can also occur in particles having a dimension much smaller than the wavelength of the light [46]. In the so called localized surface plasmon resonance (LSPR), as light interacts with a nano-particle, the particle is polarized, with an induced charge distribution appearing over the particle surface. Since the scale of the par-

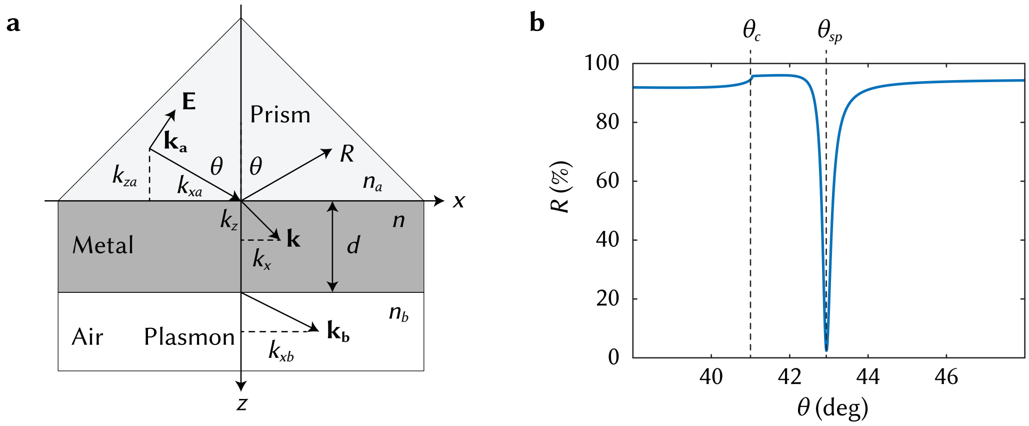

Figure 1.4 | Surface plasmon resonance excitation by total internal reflection. a, Kretschmann-Raether configuration. A thin metal film of subwavelength thickness is sandwiched between a prism and air. **b**, Reflection response for a glass-silver-air configuration with a sharp drop at the resonant angle.

ticle and the induced charge density variation can be much smaller than the wavelength, so is the local field distribution. LSPR differs from SPR as the induced plasmons oscillate locally to the nanostructure, rather than along the metal-dielectric interface. LSPR exhibit a tunable resonant frequency that doesn't require momentum matching but rather depends on the nanoparticle size, shape, composition and surrounding media.

1.2.2 Fundamentals of Guided Wave Optics

A beam of light with a finite transverse dimensions will diverge as it propagates in a homogeneous medium [47]. Generally, the beam can be confined by employing a dielectric medium of higher refractive index on the basis of total internal reflection (TIR). The confined electromagnetic propagation manifests itself in terms of guided modes supported by waveguide structures. The optical modes are solutions of the eigenvalue equation, which is derived from Maxwell's equations subject to the boundary conditions imposed by the waveguide geometry and materials.

Optical waveguides are the key components in integrated optical circuits [48]. Generally, the waveguides consist of a rectangular core surrounded by lower refractive media and confined in both transverse dimensions. However, rigorous three dimensional numerical analysis is required to obtain the transmission characteristics of such geometries. Therefore, we focus on slab waveguides which confine the mode in a single transverse dimension to acquire a fundamental understanding of optical waveguides.

1.2.2.1 The Dielectric Slab Waveguide

Optical waveguides consist of a core, in which light is confined, sandwiched between a cladding and a substrate, as shown in Fig. 1.5a. The refractive index of the waveguide core n_w is higher than of the adjacent cladding n_c and substrate n_s. Therefore, a light beam that is coupled into the waveguide is confined in the core by TIR from both interfaces and propagates in the $\hat{z}$ direction. Fig. 1.5b shows

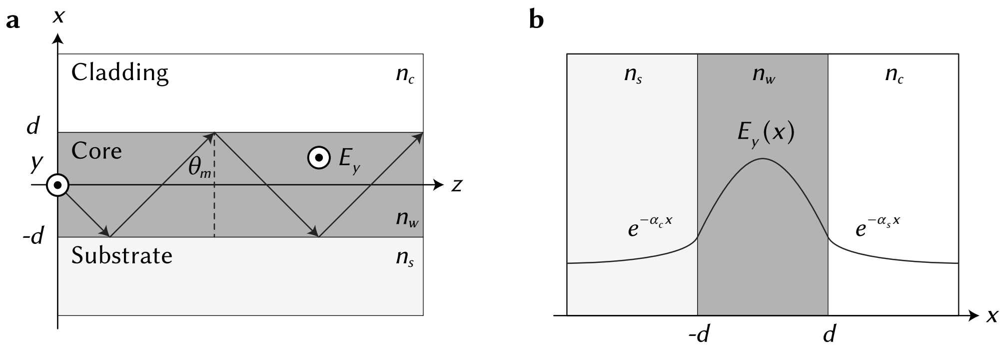

Figure 1.5 | Dielectric slab waveguide. **a**, Schematic of the dielectric slab waveguide. Light is confined in the core and propagates in the $\hat{z}$ direction. **b**, Typical electric field pattern of a propagating mode. The mode is primarily confined inside the core and decays exponentially with distance.

typical electric field profile of a waveguide mode, where the propagating fields are confined primarily inside the core. However, they also exist as evanescent waves outside of it, decaying exponentially with distance from the slab with decay constants α_s and α_c.

1.2.2.2 Guided Modes

The solution of Maxwell's equations under the appropriate boundary conditions for the waveguide shown in Fig. 1.5 requires that only certain discrete values of the propagation constant β_m are allowed [48]. Thus, there are only a limited number of guided modes in the allowed range of β

$$n_c \leq n_s \leq \frac{\beta}{k_0} \leq n_w \tag{1.12}$$

where the lower limit $\beta = k_0 n_s$ defines the cutoff frequencies. The total amount of allowed modes M are labeled by their corresponding mode number $m = 0, 1, 2, ..., M-1$. The mode number of each mode is associated with light rays at a distinct angle of propagation. The discrete modes form an orthonormal set and satisfy the wave equation.

The wave equation for the structure consists of two explicit expressions for each of the independent electromagnetic propagation modes, denoted as transverse electric (TE) and transverse magnetic (TM) modes, respectively. The characteristic normalized solution for an asymmetric slab with core thickness of $2d$ for each set of modes is

$$\begin{aligned} u &= \begin{cases} \frac{1}{2}m\pi + \frac{1}{2}\arctan\left(\frac{u}{v}\right) + \frac{1}{2}\arctan\left(\frac{w}{u}\right) & \text{TE Modes} \\ \frac{1}{2}m\pi + \frac{1}{2}\arctan\left(\frac{n_w^2}{n_s^2}\frac{u}{v}\right) + \frac{1}{2}\arctan\left(\frac{n_w^2}{n_c^2}\frac{w}{u}\right) & \text{TM Modes} \end{cases} \\ u^2 + v^2 &= V^2 , \quad w^2 - v^2 = \gamma V^2 , \quad \gamma = \frac{n_s^2 - n_w^2}{n_w^2 - n_s^2} \end{aligned} \tag{1.13}$$

where the normalized frequency V, and the transverse wavenumbers u, v and w are given by

$$V = k_0 d\sqrt{n_w^2 - n_s^2} = \frac{2\pi d}{\lambda}\sqrt{n_w^2 - n_s^2} , \quad u = k_w d , \quad v = \alpha_s d , \quad w = \alpha_c d \tag{1.14}$$

Solving Eq. (1.13) provides the propagation constant β, or equivalently, the effective mode index $n_{\text{eff}} = \beta/k_0$ using

$$\beta = \sqrt{k_0^2 n_w^2 - k_w^2} \longrightarrow n_{\text{eff}} = \frac{\beta}{k_0} = \sqrt{n_w^2 - \frac{k_w^2}{k_0^2}} = \sqrt{n_w^2 - \frac{u^2}{k_0^2 d^2}} \tag{1.15}$$

The modes in Eq. (1.13) are represented by means of a universal mode dispersion curve defined in terms of the normalized propagation constant b

$$b = \frac{\beta^2 - k_0^2 n_s^2}{k_0^2\left(n_w^2 - n_s^2\right)} \tag{1.16}$$

Substituting Eq. (1.16) into Eq. (1.13) provides the form

$$2V\sqrt{1-b} = m\pi + \arctan\left(\sqrt{\frac{b}{1-b}}\right) + \arctan\left(\sqrt{\frac{b+\gamma}{1-b}}\right) \tag{1.17}$$

Fig. 1.6a depicts the dispersion curves for TE and TM modes relating the normalized frequencies V and propagation constants b for different mode orders m. The corresponding normalized electric field profiles of the TE modes are shown in Fig. 1.6b.

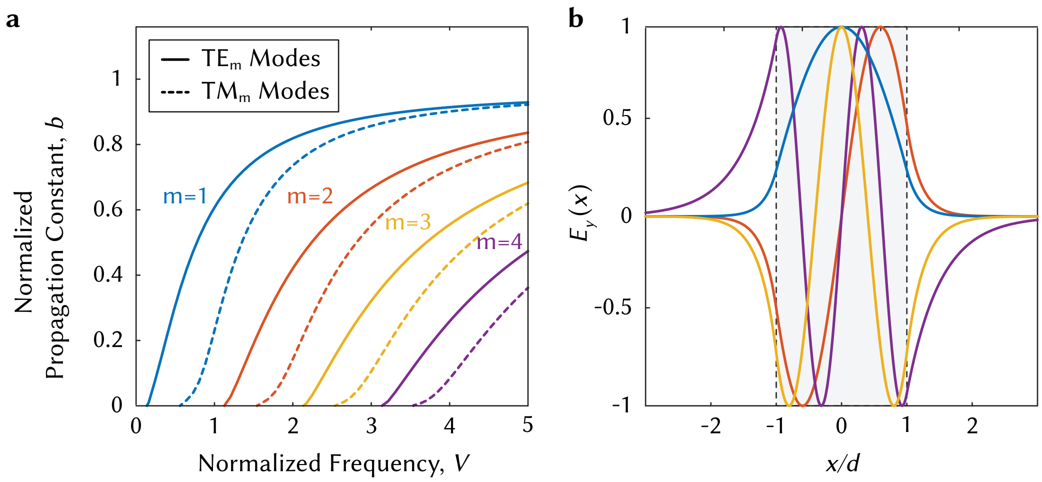

Figure 1.6 | Dispersion curves for propagating modes in a dielectric slab waveguide. **a**, Normalized propagation constant b as a function of normalized frequency V. **b**, Electric field profile of the corresponding TE modes.

1.2.2.3 Hybridization of Waveguide Modes with Plasmonic Overlayer

While the losses of dielectric waveguides can be mitigated by choosing the appropriate materials and the suitable operation wavelength, the losses of plasmonic structures are proportional to their optical mode confinement, i.e. more confined modes suffer more losses. A satisfactory compromise between the loss and confinement is achieved by depositing a thin metal film on top a dielectric waveguide to form a composite plasmonic waveguide (CPW) [49]. As a result of the large imaginary part of the metal RI, the modes of such a waveguide structure become hybrid or complex.

A detailed theoretical study of CPW and the expressions for modal expansion coefficients, optical transmittance, and surface intensity are found in [49]. The general complex EM field distributions of a CPW structure are given by

$$\begin{aligned} \mathbf{E}(x, y, z, t) &= a_m(z)\mathbf{E}_m(x, y)e^{i\left(\omega t - \beta_m z\right)} \\ \mathbf{H}(x, y, z, t) &= a_m(z)\mathbf{H}_m(x, y)e^{i\left(\omega t - \beta_m z\right)} \end{aligned} \tag{1.18}$$

where β_m is the propagation constant of the m^{th} mode, $\mathbf{E}_m(x, y)$ and $\mathbf{H}_m(x, y)$ are the transverse wavefunctions, and $a_m(z) = N_m A_m(z)$ is the complex field amplitude (CFA). The power flow in the waveguide is the sum of the power carried by each mode individually, if the power is normalized to 1W, the normalization factor of the modes can be written as

$$N_m = 2\left[\iint \Re\left(\mathbf{E}_m \times \mathbf{H}_n^*\right) dx dy\right]^{-1/2} \tag{1.19}$$

where m, n are the mode numbers of two individual modes supported by the structure.

For a given mode of propagation, the time-averaged power flow is given by

$$P = \frac{1}{2}\iint \Re[\mathbf{E} \times \mathbf{H}^*] \cdot \mathbf{a}_z da \tag{1.20}$$

The general properties of the complex waveguide modes and their energy transport relations are crucial for the design of novel waveguide devices. In the following chapeters, we will use these derivations for the characterization of our CPW.

1.3 Thesis Outline

In the preceding section, we introduced the basic theories required for the design of plasmonic and integrated photonic devices, and derived some general properties of SPPs and waveguide modes. The remainder of this thesis is organized into three main chapters.

In Chapter 2, we present the fundamental concepts and methods that were studied and used to explore subwavelength structuring in multi-layer systems and optical waveguides. We start by reviewing the principles of field concentration and enhancement in plasmonic structures. The various numerical methods we applied throughout our work are presented. We elaborate on the theory of wave propagation in different periodic media and present some of its applications in multi-layer structures and waveguides. Finally, we discuss the principles of subwavelength structures materials and how they can be used to control EM fields.

In Chapter 3, we present the major results obtained in this work. We explore the excitation of hybrid modes in dielectric and plasmonic structures, and demonstrate how the evanescent field of such a device can be manipulated to create an invisibility cloak. We present the design and implementation of metasurfaces capable of converting the eigenmodes supported by a silicon waveguide from one to another, and a metasurfaces which reduce waveguide coupling losses. In addition, the practical considerations for a novel SPR sensor are presented along with experimental results validating our design.

Finally, the main conclusions and the future prospects are described in Chapter 4. We present our research activities where materials of subwavelength dimensions are utilized for the development of novel waveguide devices and sensors.

2 Fundamental Concepts

As a fundamental property of waves, diffraction plays an important role in many physical problems. However, the phenomena of diffraction makes waves in free space unable to be focused into an arbitrarily small space, setting a fundamental limit to applications such as imaging, lithography, and guided wave optics.

The diffraction limit proposed by Ernest Abbe and Lord Rayleigh in 1870s [50] states that the resolution of microscopes and telescopes is linearly related to the wavelength and inversely related to the aperture size. Light with wavelength λ, traveling in a medium with refractive index n and converging to a spot with half-angle θ will have a minimum resolvable distance of

$$d = \frac{\lambda}{2n\sin\theta} = \frac{\lambda}{2\mathrm{NA}} \tag{2.1}$$

where $n\sin\theta$ is the numerical aperture (NA). Consequently, observing molecules with subwavelength dimensions through a microscope is very challenging [51] while exploring of life in distant planets requires huge telescope apertures [52]. Furthermore, classical absorption and emission theory of light sets a fundamental restriction on the performances of optical devices, such as bandwidth and efficiency [2].

In this chapter, we review the underlying fundamental concepts and methods used throughout this work. We primarily focus on the use of subwavelength structuring for overcoming the fundamental limitations and restrictions set by classical wave theory in several devices and applications. We explain the principles of field concentration and enhancement in plasmonic structures and discuss waveguide coupling and propagation. The essential electromagnetic analytical formulations and computational algorithms used for the design of complex subwavelength structures are presented.

2.1 Localization and Field Enhancement

In the previous chapter, we have seen that a sustained surface wave can be excited along metal surfaces accompanied by ohmic losses. The bounded solutions indicate that SPP modes are confined to the interfaces of dielectric-metal-dielectric structures. Furthermore, as seen from the dispersion relations, the propagation constant of SPP modes is larger than that of a free-space photon at a given frequency. When an EM field with frequency lower than of the SP is incident on the interface, a smaller effective wavelength for the SPP mode is achieved compared to the optical mode. This results in subwavelength confinement of light into volumes much smaller than the diffraction limit. These features of SPPs are the fundamental source for most of its applications.

The field density and lines for SPR excited in a thin film structure is shown in Fig. 2.1a. The fields are tightly bound to the surface and decay exponentially on either side of the surface. The dipole field of LSPR in a spherical nano-particle is shown in Fig. 2.1b. The polarization of the sphere lies along the polarization of the incident electric field and the field enhancement peaks on the surface.

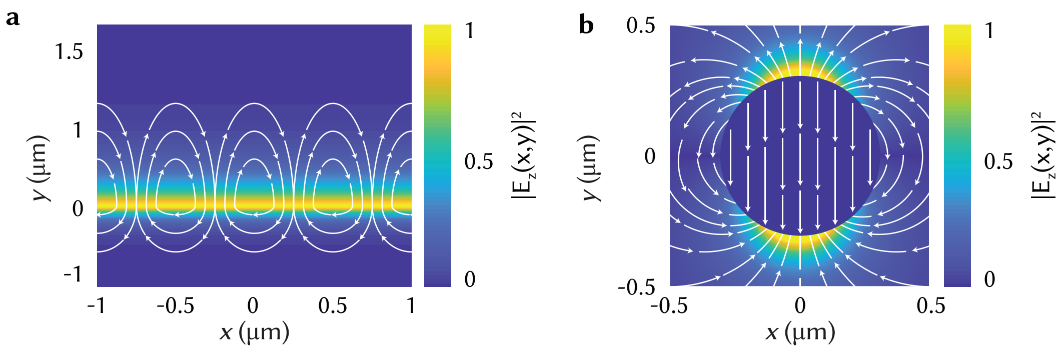

Figure 2.1 | Field localization and enhancement in plasmonic structures. a, Electric field density and lines for SPR excited in a thin film structure. The fields are bound to the surface and decay exponentially. **b**, Electric field density and lines for LSPR excited in a spherical nanoparticle. The field enhancement peaks on the surface.

This high confinement leads to significant field enhancement that can be used to manipulate light-matter interactions. The coupling mechanism, dispersion of optical modes, and the enhanced field associated with SPPs makes them suitable for a wide variety of applications, including nanophotonic devices [53], waveguides [49], and biological and chemical sensors. Based on the localized resonances and complex coupling, many novel optical functionalities, devices and systems can be realized.

2.2 Numerical Modeling

Due to the complex irregular geometries found in actual devices, several EM problems like scattering, radiation, and waveguide modeling, do not have an explicit analytical solution. Computational numerical techniques [54] can overcome the inability to derive closed form solutions of Maxwell's equations under various constitutive relations of media, and boundary conditions. This makes numerical techniques inherently vital for the design and modeling of antennas, communication systems, nanophotonic devices, medical imaging devices, and integrated optical circuits.

Typically, the numerical solution is computed in terms of the EM fields across the problem domain. The domain is subdivided into smaller regions and the resulting set of partial differential equations (PDEs) which are approximated to provide a solution across the entire space. Other merits such as power flow direction, waveguide modes, wave dispersion, and scattering can be computed from the obtained fields.

The eigenvalue problem formulation of the numerical techniques allows us to calculate steady state normal modes in a structure. While transient response and impulse field effects are more accurately modeled in time domain by the finite difference time domain (FDTD) method, curved geometrical objects and thin features are treated more accurately by the finite element method (FEM). Each method is application specific and choosing the right technique for solving a problem is important for shorter computation time and accuracy.

2.2.1 Finite-Difference

FDTD [55] is a numerical analysis technique used to find approximate solutions for the associated system of time-dependent partial differential equations (PDEs).

Since it is a time-domain method, FDTD solutions can cover a wide frequency range with a single simulation run. The FDTD method provides direct time and space solutions to Maxwell's equations in complex geometries using grid-based differential time-domain numerical modeling. The equations are modified to central-difference equations, discretized, and implemented in software.

In this work, we use the commercial package of Lumerical Finite-Difference integrated design environment (IDE) [56] to solve problems which include wave propagation in large structures. These models are large compared to wavelength and the FDTD method gives a good compromise between accuracy and computational resources.

The three-dimensional space consists of an orthogonal Cartesian grid with multiple cells constituting a set of PDEs. An illustration of a standard cell used for FDTD is shown in Fig. 2.2. The cell is visualized as a cubic voxel where the electric field components form the edges of the cube, and the magnetic field components form the normals to the faces of the cube. The EM wave interaction is implemented into the spatial grid by assigning the appropriate values of permittivity and permeability to each field component. The equations are solved in a cyclic manner, i.e., the electric field is solved at a given instant in time, then the magnetic field is solved at the next instant in time. This process is repeated until the desired transient or steady-state electromagnetic field behavior is fully evolved.

Being a direct time and space solution, FDTD offers an insight into all types of problems in electromagnetics and photonics. The frequency solution is obtained by exploiting Fourier transforms, thus a full range of useful quantities can be calculated, such as the complex Poynting vector, waveguide mode profiles and the transmission/reflection of light.

2.2.2 Finite-Element

As with the finite difference scheme, the FEM is a numerical technique that reduces problems defined in geometrical space by subdividing the domain into smaller regions to find a solution in a finite number of points. In contrast to finite difference procedures, each subregion or element is unique and doesn't require orthogonality. The governing equations in the FEM are integrated over each finite element,

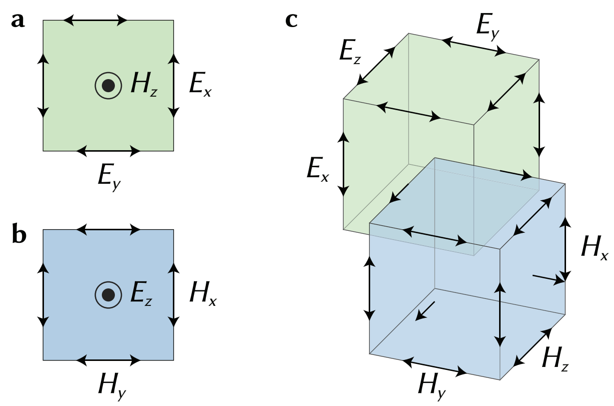

Figure 2.2 | Illustration of a standard Cartesian cell used for FDTD. a, Electric field components which form the edges of the cube. **b**, Magnetic field components which form the normals to the faces of the cube. **c**, The FDTD cell is visualized as a cubic voxel.

and the contributions are summed to assemble the solution over the entire problem domain.

FEM uses triangular and quadrilateral elements in two dimensional problems, and various polyhedrons in three dimensions. The unknown variables are approximated using known basis functions over each finite element and expressed as functions of the geometrical locations of the element nodes. Consequently, a set of finite linear equations is obtained in terms of the values of the unknown parameters at the nodes and solved using linear algebra techniques.

A typical FEM mesh showing the geometry and placement of nodes for 3D linear elements is shown in Fig. 2.3a. The domain contains complex geometry with curved edges and surfaces. A typical visualization of a FEM solution is shown in Fig. 2.3b.

One of the most important features of FEM is that it is based on unstructured grids. This means that FEM is more flexible with respect to the geometry. In this work, we use the commercial package of COMSOL Multiphysics IDE [57] as our FEM solver. Although FEM is much more computationally expensive than FDTD, we use it for simulations which include complex curved geometries and thin film structures. In addition, we use FEM for validation purposes of our FDTD simulations.

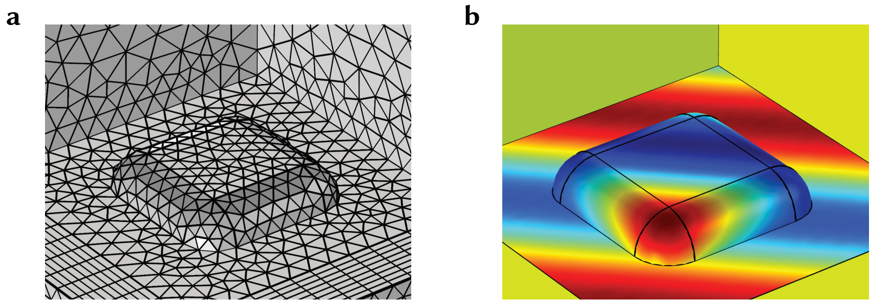

Figure 2.3 | Illustration of typical FEM mesh and solution. **a**, Mesh showing the geometry and placement of nodes for 3D linear elements. **b**, Visualization of a FEM solution.

2.3 Wave Propagation in Periodic and Layered Media

The propagation of EM radiation in periodic media exhibits many interesting and useful phenomena employed in many devices such as diffraction gratings, Bragg mirrors [58], distributed feedback lasers [59], acousto-optics [60], and plays an important role in guided-wave optics [61]. The periodicity is generally described in terms of the material optical constants being periodic functions of position. While simple structures such as layered media have closed-form solution of Maxwell's equations and can be treated using matrix formulation, perturbation theory is applied where only approximate solutions can be obtained.

In this work, we use the principles of layered media for the design of novel SPR sensor. The closed form solutions of these structures are used for optimization and characterization of the sensor. We use the perturbation theory for the design of periodic structures that convert between the propagating modes in a waveguide.

2.3.1 Periodic Layered Media

We first consider the general case of a multilayer structure consisting of homogeneous layers of different materials, where we assume that the structure consists of N layers and the wave propagates in the $\hat{z}$ direction. The fields traveling in the backward and forward directions in the i^{th} layer can be expressed in a matrix form in terms of a unit-cell translation matrix relating the CFAs of the plane waves between the layers

$$\begin{bmatrix} E_i^+ \\ E_i^- \end{bmatrix} = \frac{1}{1+r_i} \begin{bmatrix} e^{ik_i l_i} & r_i e^{-ik_i l_i} \\ r_i e^{ik_i l_i} & e^{-ik_i l_i} \end{bmatrix} \begin{bmatrix} E_{i+1}^+ \\ E_{i+1}^- \end{bmatrix} \tag{2.2}$$

where r_i is the elementary reflection coefficient from the right side of each interface, and $k_i l_i = 2\pi n_i l_i/\lambda$ is the phase thickness of each layer.

The reflection response of the i^{th} layer is given by

$$R_i = \left| \frac{r_i + R_{i+1} e^{2ik_i l_i}}{1 + r_i R_{i+1} e^{2ik_i l_i}} \right|^2 \tag{2.3}$$

the total reflection response of an arbitrary structure with N cascaded layers can be calculated recursively using Eq. (2.3).

Next, we consider a periodic medium consisting of alternating layers of air with RIs n_a and n_b, thicknesses l_a and l_b, respectively, and period $\Lambda = l_a + l_b$. The structure shown in Fig. 2.4a is known as a dielectric mirror (also Bragg reflector) and the layer thicknesses are typically chosen to be quarter-wavelength long, that is, $n_a l_a = n_b l_b = \lambda_0/4$. The total reflection response for this structure is given by

$$R = \left| \frac{1 - \left(\dfrac{n_b}{n_a}\right)^{2N}}{1 + \left(\dfrac{n_b}{n_a}\right)^{2N}} \right|^2 \tag{2.4}$$

The normalized reflection response for several values of N layer pairs is plotted in Fig. 2.4b. The parameters used for the calculations are $n_a = 1$, $n_b = 1.52$, $\lambda_0 = 1.55$ µm, $l_a = \lambda_0/4n_a$, and $l_b = \lambda_0/4n_b$. The reflectivity increases with the amount of periods. It follows that for large N, the reflection will tend to 100%.

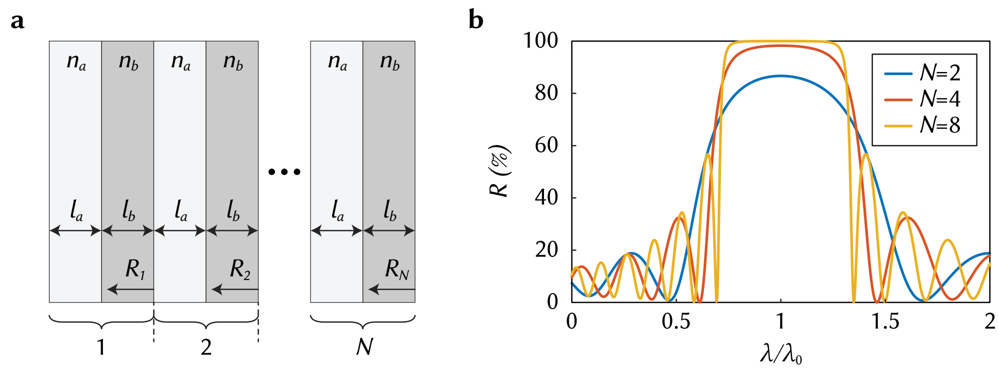

Figure 2.4 | Periodic layered medium schematic and reflection response. a, The periodic layered structure consisting of alternating layers of two materials. **b**, Normalized reflection response of the structure. The reflection increases with the amount of periods.

2.3.2 Coupled Mode Theory and Periodic Waveguides

In spite of the fact that the exact solutions for EM propagation in a periodic layered medium can be easily obtained, there many periodic media where only approximate solutions are available. In this case, the periodic variation of the dielectric tensor is considered as a perturbation that couples the unperturbed normal modes of the structure and treated using the coupled mode theory (CMT) [61]. We use the CMT for the analysis of the interaction between the guided modes in optical waveguide devices.

The electric fields in the perturbed waveguide can be written using the superposition of all the possible $\mathbf{E}_m(x, y)$ eigenmodes in the unperturbed waveguide as

$$\mathbf{E}(x, y, z, t) = \sum_{m=1}^{M} A_m(z)\mathbf{E}_m(x, y)e^{i(\omega t - \beta_m z)} \tag{2.5}$$

where m is the mode order, $A_m(z)$ is the CFA, β_m is the propagation constant of the m^{th} guided mode in the propagation direction $\hat{z}$ and ω is the angular frequency.

The transverse wavefunctions $\mathbf{E}_m(x, y)$ satisfy the unperturbed wave equation and form an complete orthonormal set such that

$$\iint \mathbf{E}_n^*(x, y)\mathbf{E}_m(x, y)dxdy = \frac{2\omega\mu}{|\beta_m|}\delta_{mn} \tag{2.6}$$

We now consider the effect of a dielectric perturbation $\Delta\varepsilon(x, y, z)$. The spatial dielectric tensor can be written as

$$\varepsilon(x, y, z) = \varepsilon_a(x, y, z) + \Delta\varepsilon(x, y, z) \tag{2.7}$$

where ε_a is the unperturbed part of the dielectric tensor and $\Delta\varepsilon(x, y, z)$ represents the periodic dielectric perturbation along $\hat{z}$. We further assume that the dielectric perturbation is weak compared to the index of the waveguide core so that the variation of the mode amplitudes satisfies the slowly varying amplitude (SVA) approximation [62]

$$\frac{d^2}{dz^2}A_m \ll \beta_m \frac{d}{dz}A_m \tag{2.8}$$

Since the perturbation $\Delta\varepsilon(x, y, z)$ is chosen to be periodic in z, we can expand it into Fourier series

$$\Delta\varepsilon(x, y, z) = \sum_{k\neq 0} \Delta\varepsilon^{(k)}(x, y)e^{-i\left(\beta_m - \beta_n\right)z} \tag{2.9}$$

where $\Delta\varepsilon^{(k)}(x, y)$ is the k^{th} Fourier coefficient of the perturbation.

Solution of the wave equation using the expressions provided above consists of a set of coupled linear differential equations according to the number of all possible eigenmodes M

$$\sum_m^M \frac{d}{dz}A_m = -i\frac{\beta_m}{\left|\beta_m\right|}\sum_{k\neq 0}\sum_n^M \kappa_{mn}^{(k)}A_n(z)e^{-i\left(\beta_m - \beta_n\right)z} \tag{2.10}$$

where $A_m(z)$ and $A_n(z)$ are the normalized CFAs along the propagation direction z, β_m and β_n are the propagation constants of the modes with transverse electric field profiles $\mathbf{E}_m(x, y)$ and $\mathbf{E}_n(x, y)$.

These coupled mode equations relate the amplitudes of each possible modes in the waveguide in terms of the coupling coefficients $\kappa_{mn}^{(k)}$ defined as

$$\kappa_{mn}^{(k)}(z) = \frac{\omega}{4} \int\int \mathbf{E}_m^*(x,y)\Delta\varepsilon^{(k)}(x,y,z)\mathbf{E}_n(x,y)dxdy \tag{2.11}$$

$\kappa_{mn}^{(k)}$ reflects the magnitude of the coupling between the m^{th} and n^{th} modes due to the k^{th} Fourier component of the dielectric perturbation $\Delta\varepsilon(x,y,z)$.

In principle, for a waveguide supporting M modes, all the mode amplitudes are involved, and in the presence of a change in the waveguides cross section, optical modes can either couple or interfere with each other. However, in practice, only two modes are strongly coupled and Eq. (2.10) reduces to a set of two equations for the two mode amplitudes. Two modes are strongly coupled when the phase matching condition is satisfied

$$\beta_m - \beta_n - p\frac{2\pi}{\Lambda} = 0 \longrightarrow \Lambda = p\frac{\beta_m - \beta_n}{2\pi} = p\frac{\Delta\beta}{2\pi}\ , \quad p = 1,2,3,...,M \tag{2.12}$$

This is the fundamental condition where coupling between two modes can occur. It is chosen as to compensate for the propagation constant mismatch of the two modes.

CMT is inherently directional. If two forward moving waves are strongly coupled, then their interactions with the corresponding backward waves may be ignored. Similarly, if a forward and a backward moving wave are strongly coupled, then their interactions with the corresponding waves in the opposite direction may be ignored.

The differential equations describing the coupling of two modes are given by

$$\frac{d}{dz}\begin{bmatrix} A_m(z) \\ A_n(z) \end{bmatrix} = -i\begin{bmatrix} \beta_m/\left|\beta_m\right| & \kappa_{mn}e^{-i\Delta\beta z} \\ -\kappa_{nm}e^{i\Delta\beta z} & -\beta_n/\left|\beta_n\right| \end{bmatrix}\begin{bmatrix} A_m(z) \\ A_n(z) \end{bmatrix} \tag{2.13}$$

The mode powers as a function of distance L for a co-directional coupler are plotted in Fig. 2.5a. When the two coupled modes are propagating in the same forward direction, i.e. $\beta_m\beta_n \geq 0$, the power carried by mode m can be exchanged with the power in mode n. Complete power transfer occurs only when the phase matching condition is fully satisfied (i.e. $\Delta\beta = 0$) and represented by the solid curves. When $\Delta\beta \neq 0$, represented by the dashed lines, only some of the power is coupled between the modes.

In conra-directional coupling, i.e. $\beta_m\beta_n \leq 0$, the backward wave is generated by the reflection of a forward-moving wave incident on the interface from the left. The periodic perturbation behaves very similarly to a periodic multilayer structure, such as a dielectric mirror at normal incidence, exhibiting high-reflectance bands, and the mode power decreases exponentially with distance as plotted in Fig. 2.5b.

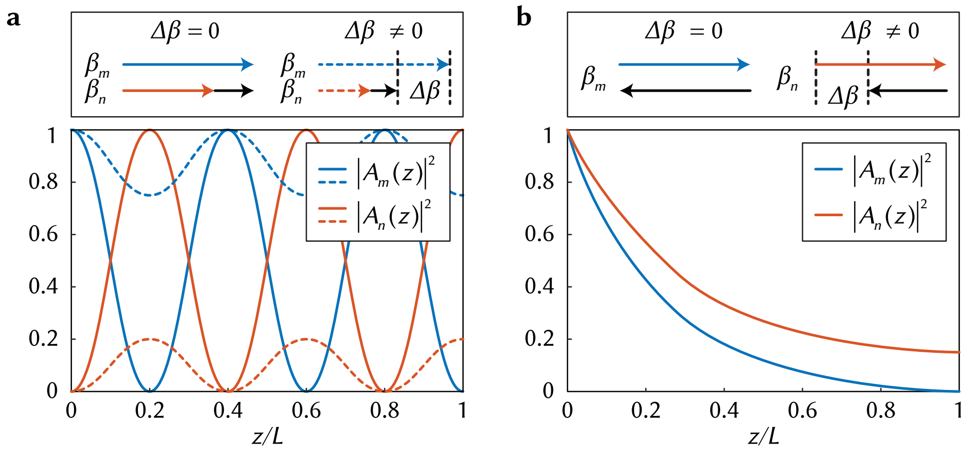

Figure 2.5 | Mode powers and phase diagrams for waves traveling in a perturbed waveguide. **a**, Co-directional coupled modes. The modes exhibit periodic power exchange. Complete power exchange occurs when the phases are perfectly matched. **b**, Contra-directional coupled modes. The mode powers decrease exponentially with the distance.

2.4 Subwavelength Structured Materials

In principle, most of the subwavelength structured materials can be classified into two categories, i.e., the periodic and gradient structures. The arrangement of subwavelength structures enables the control of material parameters such as permittivity, permeability, and impedance. These kinds of effective materials are widely known as metamaterials [13, 63].

2.4.1 Metamaterials and Metasurfaces

The precise shape, geometry, size, orientation and arrangement of the subwavelength structures gives metamaterials the capability of manipulating electromagnetic waves by blocking, absorbing, enhancing, or bending waves, to achieve benefits that go beyond what is possible with conventional materials.

Generally, metamaterials can be treated as effective media, where their extraordinary properties depend on their structure rather than their composition. Each unit cell in a metamaterial is significantly smaller than the wavelength of interest. Therefore, each unit can be viewed as a microscopic building block of the metamaterial, in analogy to the atoms in the naturally occurring conventional materials.

Compared with 3D metamaterials, 2D subwavelength structures, or metasurfaces, are much easier to design and fabricate. Periodic metasurfaces are widely used as spectral filters [64], perfect absorbers [65], and polarization converters [66]. While gradient metasurfaces can be used for flat focusing [67], beam splitting, and holography [68].

2.4.2 Optical Cloaking

One of the most appealing applications of metamaterials is possibility of making objects invisible to the incoming EM radiation. Practically, the cloaking effect aims at canceling the EM fields that are scattered by an object. Ideally, cloaking an object implies total scattering suppression from all angles, independently of the environment, or the position of the observer, and over a wide frequency range, with the ultimate goal of all-angle invisibility over the entire visible range. However, several fundamental challenges arise when realizing such an ideal device [69].

In this work, we use the transformation optics (TO) technique to design an evanescent field waveguide cloak which conceals an object located on top of a waveguide. Transformation-based cloaking applies the concept of TO to manipulate the flow of electromagnetic energy using a transformation that stretches the coordinate grid of space, as shown in Fig. 2.6b. By stretching and compressing the Cartesian space, one can bend the ray at will and control its propagation, similar to what is originally speculated in Fermat's principle. The coordinate transformation in the physical space is practically controlled via the material parameters.

An alternative TO based cloaking scheme is the quasi-conformal transformation optics (QCTO) [70], where the anisotropy is minimized in a two dimensional coordinate transformation by applying an optimization procedure. Such transformations may be implemented in a broadband way at visible frequencies. As a result, the very weak anisotropy of the resulting media may be neglected, obtaining isotropic graded index (GRIN) cloaks.

2.4.3 Transformation Optics

The TO technique is used to mimic the space curvature in general relativity with gradient materials [71], allowing the design of complex gradient optical devices with exotic properties such as invisibility [16], and arbitrary beam shaping [72]. It is built upon the form-invariance of Maxwell's equations under coordinate transformations. As a result, the interpretation of Maxwell's equations in different coordinate systems is equivalent to changing the medium parameters in the constitutive relationships.

In the three-dimensional Euclidean space, the coordinate transformation between the original Cartesian system (x, y, z) and the transformed system (x', y', z') is related by the Jacobian matrix $\mathbf{A}$

$$\mathbf{A} = \begin{bmatrix} \partial x'/\partial x & \partial x'/\partial y & \partial x'/\partial z \\ \partial y'/\partial x & \partial y'/\partial y & \partial y'/\partial z \\ \partial z'/\partial x & \partial z'/\partial y & \partial z'/\partial z \end{bmatrix} \tag{2.14}$$

Consequently, both field and medium quantities in the (x', y', z') system are related to their respective counterparts in the (x, y, z) system. The medium tensor parameters, $\bar{\mu}'$ and $\bar{\varepsilon}'$, are related to $\bar{\mu}$ and $\bar{\varepsilon}$ in the original space by the following expressions

$$\bar{\mu}' = \frac{\mathbf{A}\bar{\mu}\mathbf{A}^T}{\det \mathbf{A}} \quad , \quad \bar{\varepsilon}' = \frac{\mathbf{A}\bar{\varepsilon}\mathbf{A}^T}{\det \mathbf{A}}. \tag{2.15}$$

Eqs. (2.15) are known as the materials interpretation of the coordinate transformation which allows electromagnetic phenomena envisioned in the transformed space to be realized in real space using the transformation media. Hence, designing a device that performs a given novel function reduces to finding an appropriate coordinate mapping that realizes it in the transformed space. This process provides an unprecedented control over wave-material interactions.

Two examples of TO based devices are shown in Fig. 2.6. Fig. 2.6a shows a flat lens designed using TO. The original Cartesian space is initially mapped into curved space representing the lens, the material properties in the original domain are calculated according to the prescribed transformation, and as a result, a geometrically flat lens is able to diverge in incoming Gaussian beam. In the second example shown in Fig. 2.6b, a cylindrical cloak is demonstrated. The fields produced by a line source outside the cloaked region are not influenced by the cloak embedded in the center.

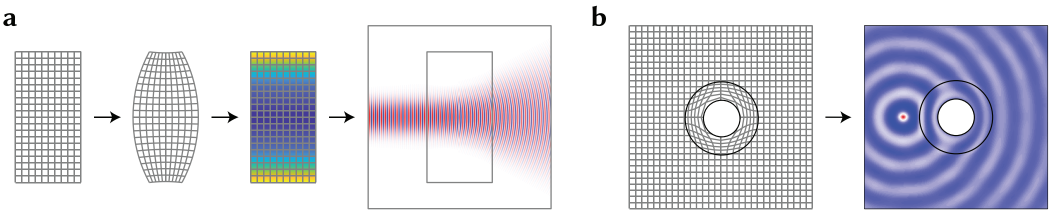

Figure 2.6 | Examples of devices employing the transformation optics technique. **a**, A flat behaves as a conventional spherical lens based on the transformed materials and diverges an incident Gaussian beam. **b**, A cylindrical cloak is unaffected from waves incoming from a line source outside the cloaked region.

The construction of transformation media for the TO designs discussed above normally requires anisotropic and inhomogeneous metamaterials with extreme parameters, which give rise to narrow bandwidths and high intrinsic losses. These difficulties limit the applications of TO based devices. The design of a real device requires relaxation the extreme requirements on material properties in order to practicably use the power of transformation optics to design exotic optical devices. One solution for the relaxation of the material properties is the QCTO scheme [70].

Specifically, in cloaking, straightforward compression of space in the physical domain essentially makes the cloak anisotropic. However, the QCTO approach is to minimize the induced anisotropy by choosing a suitable coordinate transform. If the anisotropy is small enough, we can simply drop it and only keep the refractive index n which is defined relative to the reference medium n_r by

$$n = n_\mathrm{r}\frac{1}{\sqrt{\det g}} \tag{2.16}$$

In other words, the physical medium becomes just a dielectric profile with unit magnetic permeability and the covariant matrix g given by

$$g = \mathbf{A}^T\mathbf{A} \tag{2.17}$$

If there is a very fine rectangular grid in the virtual domain with cells of size $\delta \times \delta$, every cell is transformed into a parallelogram in the physical domain. A smaller anisotropy means a smaller value of $\mathrm{Tr}(g)/\sqrt{\det g}$, while a smaller area of the transformed cell $\sqrt{\det g}\delta^2$ means a larger refractive index n. The optimal map of a domain with length L and width w is generated by minimizing the Modified-Liao functional [73]

$$\Phi = \frac{1}{Lw}\int_0^L dz' \int_0^w dx' \frac{\mathrm{Tr}(g)^2}{\det g} \tag{2.18}$$

and satisfying the Cauchy–Riemann conditions [74] given by

$$\frac{\partial x'}{\partial x} = \frac{\partial z'}{\partial z} \quad , \quad \frac{\partial x'}{\partial z} = -\frac{\partial z'}{\partial x} \tag{2.19}$$

Thus, the term $\mathrm{Tr}(g)/\sqrt{\det g}$ depends on the aspect ratio of each transformed cell and is called the anistropy factor. The design goal is to achieve constant anisotropy throughout the entire mesh by orthogonalizing the grid lines.

In contrast to general embedded TO designs, the QCTO components contain materials that can be implemented with standard fabrication techniques, facilitating their application and integration into on-chip photonic systems [75]. By exploiting the flexibility of the QCTO approach, compact GRIN components can provide superior performance compared to their state-of-the-art counterparts. Furthermore, the TO components can introduce new functionalities to conventional GRIN optics and significantly improve the system level integration of photonic devices. In this work, we use the QCTO technique for the design of an evanescent field waveguide cloak.

2.4.4 Effective Medium Theory

The effective medium theory (EMT) is used to describe the macroscopic properties of composite materials [76]. It is developed from averaging the multiple values of the properties of the subwavelength structures that directly make up the composite material. At the subwavelength scale, the values of the materials spatially vary and are inhomogeneous. The effective medium approximations are descriptions of a metamaterial based on the properties and the relative fractions of its components, and are derived from calculations. In this work, we use the EMT in order to physically interpret the calculated material properties provided by the TO technique and the periodic RI distributions for the design of waveguide mode converters.

The effective permeability and permittivity tensors $\bar{\mu}$ and $\bar{\varepsilon}$ of a medium consisting of subwavelength cells of isotropic materials behaves based as if it is homogeneous but anisotropic when the structures are sufficiently small. Suppose we have a medium consisting of alternate layers of thicknesses a and b. We are interested in the field averaged over the period $\Lambda = a + b$ of such a structure. The introduction of this average field evidently has significance only under the condition that its change over a distance Λ is sufficiently small along any arbitrary direction of propagation. This condition can he formulated as

$$k\Lambda|n| \ll 1 \tag{2.20}$$

where $k = \omega/c = 2\pi/\lambda$, and n is the effective RI tensor of the medium, different for every direction of propagation and for different polarizations. For sufficiently long waves, the effective properties of the medium are especially simple. That is, the inhomogeneous isotropic medium under consideration then behaves, with respect to the average field, like a homogeneous but anisotropic medium, i.e., the effective permeability and permittivity are singly degenerate tensors. The possibility of artificially constructing anisotropic materials of the indicated type and varying their electromagnetic properties is of great interest and is the main principle behind metamaterials.

3 Results and Discussion

In the preceding chapters, we presented the theories and the fundamental concepts of optical waveguides and SPs. The various techniques previously described were applied for the design of novel devices employing materials of subwavelength dimensions. The main results for the projects are presented in this chapter.

3.1 Evanescent Field Waveguide Cloaking

SPPs are widely used in various applications due to their resonant behavior and ability to confine field in a subwavelength scales. It is known, that SPP is a surface wave propagating along a metal-dielectric interface. The main property of SPPs is strong localization of electric field with a maximum at the interface. However, one of the significant disadvantages of SPPs is a relatively high dissipation that essentially limits their applications.

In this work, we explore the excitation of hybrid modes in the two-dimensional dielectric waveguide based on a metal film located on its top to combine the properties of photonic and plasmonic structures in the so called CPW. We demonstrate the control of the behavior of SPPs propagation exited at this interface using a metasurface designed with the TO technique. The calculated effective index which produces an evanescent field cloak on top of a CPW is numerically implemented and we show how the evanescent fields are directed around a cylindrical object and thus concealing it. We suggest a method of physical implementation of the device by physically interpreting the material parameters by varying the thickness of a dielectric film.

3.1.1 Composite Plasmonic Waveguides

The operation of the CPW can be explained using the concept of mode coupling. It consists of thin metal film deposited on a conventional strip waveguide. On the one hand, the dielectric waveguide supports guided modes which are mostly confined inside the dielectric guiding layer. On the other hand, the metal surface supports SPP modes, which are confined near the metal surface. When these two structures are brought together, the dielectric waveguide mode couples to the SPP mode supported by the metal surface. As a result of this mode coupling, light becomes highly confined in the region of the metal-dielectric interface.

To further confine the field in the top of the waveguide, we introduced an additional Si overlayer on the CPW. This leads to strong field localization in the Au-Si interface and more energy present in the SPP part of the hybrid modes. This hybridization between plasmonic and dielectric modes leads to tight mode confinement in the plane perpendicular to the propagation direction. We utilize this property for the design of the evanescent field waveguide cloak.

Consider the guided wave system shown in Fig. 3.1. A gold ($n_{\mathrm{Au}} = 0.182 + i3.068$ [77]) strip with length of L =10 µm and thickness d_{Au} = 40 nm, is introduced on top of a Si_3N_4 (n_{Si3N4}=2.02 [78]) waveguide with width w_{wg} = 800 nm and height h_{wg} = 400 nm to form a high index CPW structure on a SiO_2 (n_{SiO2} = 1.457 [77]) substrate. In order to confine the optical mode in vicinity with the metal-dielectric interface and for the efficient coupling to the surface plasmon modes, silicon (n_{Si} = 3.882 + i0.019 [77]) nano-spacer with thickness d_{Si}=10 nm is placed on top of the metasurface. The CPW structure is longitudinally confined in between the abrupt steps I and II and illuminated the TM_0 mode at the wavelength λ = 632.8 nm.

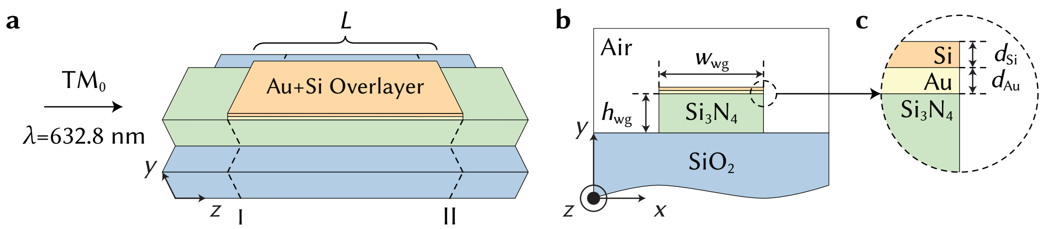

Figure 3.1 | Geometry and structure of a composite plasmonic waveguide. a, 3D schematic of the CPW structure; thin strips of gold and silicon are deposited on top of Si_3N_4 waveguide to allow the support of both dielectric and plasmonic modes. **b**, Transverse cross-sectional view (xy plane) of waveguide. **c**, Magnified view of the overlayer deposited on top of the waveguide core.

Our theoretical analysis is based on the semi-analytical model of orthonormalization of complex eigenmodes at an abrupt step, developed for the investigation of the transmission and surface intensity in CPW structures in [49]. The numerically calculated electric field profiles of the $\hat{z}$ component of the electric field of the modes, $\left|E_z(x, y)\right|^2$, supported by each section of the structure are shown in Fig. 3.2. The TM_0 dielectric mode (DM) supported in the regions $z < -L/2$ and $z > L/2$ is shown in Fig. 3.2a. This mode is used as the input and propagates in the dielectric section up to the first step of discontinuity with the CPW section. The eigenmodes after this step are not pure dielectric anymore and SPP modes such as the symmetric SPP mode (SPP-s) shown in Fig. 3.2b can exist in the region $-L/2 \leq z \leq L/2$. As the DM reaches the discontinuity step, part of the light is coupled out of it and into the SPP mode resulting in an hybrid dielectric mode (HDM) shown in Fig. 3.2c. The field amplitudes at the middle of the waveguide $\left|E_z(x = 0, y)\right|^2$ are shown in Fig. 3.2d.

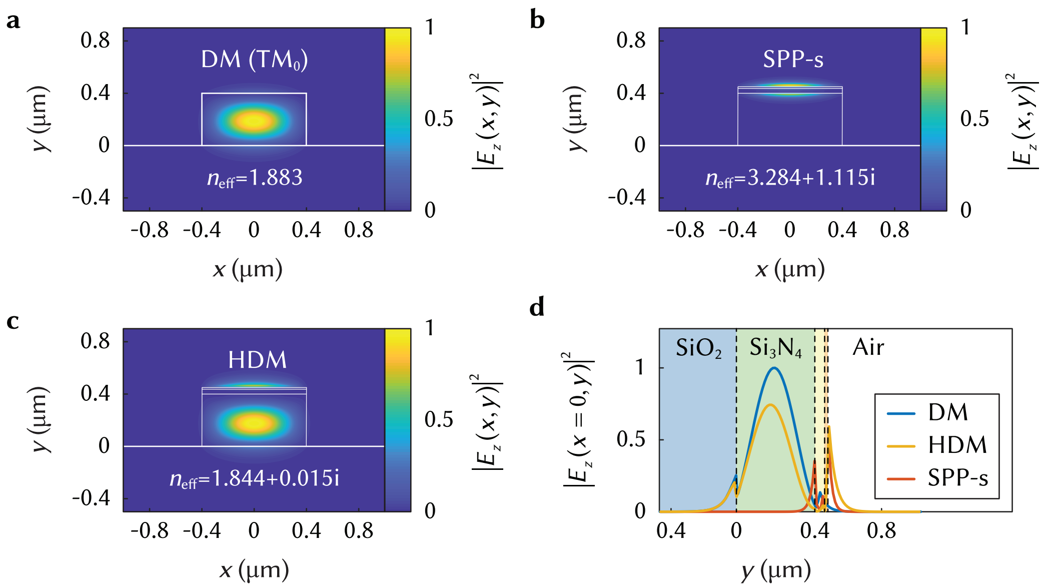

Figure 3.2 | Calculated electric field profiles of the modes supported by the composite plasmonic waveguide. **a**, Dielectric mode (DM) which is the TM_0 mode supported by the waveguide. **b**, Symmetric SPP (SPP-s) mode supported by the CPW. **c**, Hybrid dielectric mode (HDM) as a result of the coupling between the dielectric and plasmonic mode. **d**, Field amplitudes at the middle of the waveguide.

The EM fields of the modes depends on the optical properties of a waveguide structure and materials. They are localized in different areas of the waveguide. The input is illuminated by the DM mode, which is the fundamental TM polarized guided mode supported by the waveguide. Between the steps of discontinuity, a resonance occurs when the DM and SPP-s modes are phase-matched in terms of propagation constant resulting in the HDM.

3.1.2 Cloak Design

In our design, we use the TO technique to transform the coordinates of the Si nano-spacer in the CPW and calculate the required material parameters to form a metasurface which routes the evanescent field around a cloaked region. In plasmonics, since the most energy is carried in the evanescent field outside the metal, it is rational to control SPPs by only modifying the dielectric material, while keeping the metal property fixed.

The transformed region is a two-dimensional rectangle with length L and width w_{wg} corresponding to the dimensions of the CPW section in the waveguide (see Fig. 3.1). The area is bounded by $-L/2 \leq z \leq L/2$ and $-w_{\mathrm{wg}}/2 \leq x \leq w_{\mathrm{wg}}/2$. The region is initially mapped into an orthogonal Cartesian mesh represented by black grid in Fig. 3.3a. The grid contains 250×20 equivalent area cells with side lengths of $\delta = 40$ nm (see Fig. 3.1). Since the system is symmetric along x, we calculate the transformation for the positive $x > 0$ half space and reflect the result in the $x < 0$ region.

In order to form the cloaked region, the inner boundary of the cloak is initially mapped according to

$$x(z) = \begin{cases} \frac{w_{\mathrm{c}}}{2}\cos^2\left(\frac{\pi z}{l_{\mathrm{c}}}\right) & -\frac{l_{\mathrm{c}}}{2} \leq z \leq \frac{l_{\mathrm{c}}}{2} \\ 0 & \text{otherwise} \end{cases} \tag{3.1}$$

where $w_c = w_{\mathrm{wg}}/2 = 0.4$ µm, and $l_{\mathrm{c}} = 4$ µm, are the width and length of the cloak, respectively. The transformed area in Fig. 3.3b becomes the cloak later.

Fig. 3.3b shows the transformed grid and the corresponding reference RI $n_r(x, z)$ in the physical system if simple transfinite interpolation is used, i.e, a linear compression in the $\hat{x}$ direction. Since this grid is non-orthogonal and the cells have different aspect ratios, the resulting material parameters are highly anisotropic. Nevertheless, this mapping serves as an initial guess for the next step of our design.

Next, we turn to orthogonalization of the grid. As previously stated, our problem objective is minimizing the expression in Eq. (2.18) while satisfying the constraints in Eq. (2.19) and the boundary conditions prescribed by the edges of our domain. The problem constitutes a set of discrete partial elliptic differential equations. These equations are numerically solved in MATLAB using an iterative algorithm based on the successive over relaxation (SOR) method [79]. As a result, the aspect ratio of each cell or the anisotropy factor becomes a constant. The maximum of n occurs on the inner cloak boundary where the cell area is largest. Therefore, we sacrifice n to a larger range while the anisotropy is minimized resulting in the spatial RI profile shown in 3.3c.

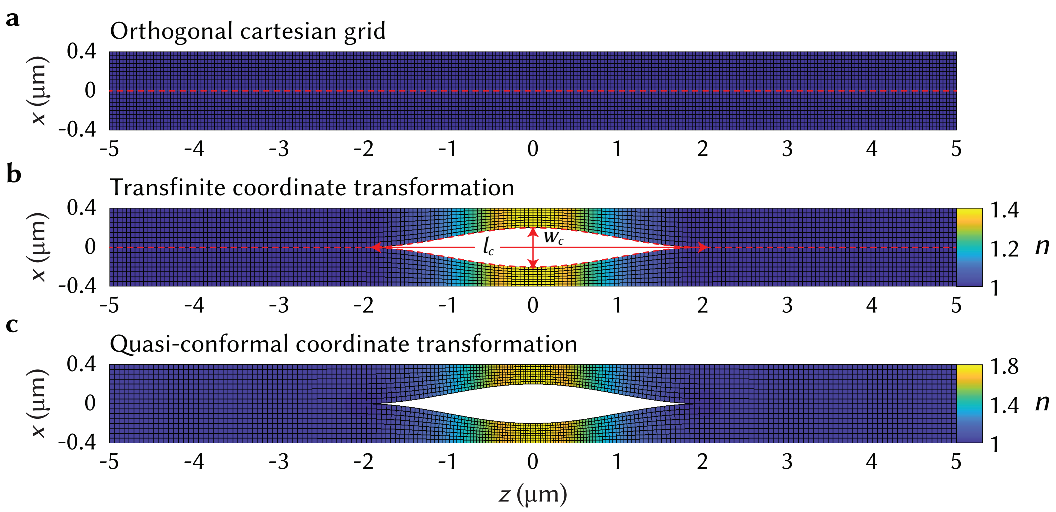

Figure 3.3 | Transformed grids and refractive index of the evanescent field waveguide cloak. **a**, Orthogonal Cartesian grid representing the discretized metasurface. **b**, Grid and RI profile of a transfinite transformation. **c**, Optimized Quasi-Conformal transformation used for the implementation of our device.

3.1.3 Evanescent Field Cloaking

As previously stated, if we rigorously follow the TO approach, both the metal and dielectric materials have to undergo a coordinate transformation to modify the propagation of SPPs. However, since most of the SPP modes energy resides in the dielectric media above the metal layer, as shown in Fig. 3.2d, transforming only the dielectric medium is sufficient to mold the propagation of SPPs [80].

To confirm the cloak operation, we implemented the RI profile as a linear relation with the refractive index of the silicon overlayer and preformed full wave simulations to obtain the 3D EM fields of the structure. In order to assess the effectiveness of the evanescent invisibility cloak, we use the surface intensity $\mathbf{I}$ on top of the silicon layer. The integrated surface intensity $\mathbf{I}$ over a waveguide width w_{wg} and along the interaction length L in the propagation direction $\hat{z}$ is given by

$$\mathbf{I} = \left| \sum_{m=1}^{M} \mathbf{E}_m(x, y_s, z) \right|^2 \tag{3.2}$$

where m is the mode index of the M supported modes in the region $-L/2 \leq z \leq L/2$ with the corresponding calculated electric field profile $\mathbf{E}_m$ and $y_s = h_{\mathrm{wg}} + d_{\mathrm{Si}} + d_{\mathrm{Au}}$.

Fig. 3.4 shows the normalized intensity maps of for four different cases. In order to obtain a reference for the cloaking results, we first calculated the fields in the system without any modification as shown in Fig. 3.4a. Fig. 3.4b show the intensity with an object of cylindrical shape with radius r = 400 nm and RI n = 1.3 located on top of the overlayer. The object scatters the incoming wave as a result of the interaction with evanescent fields.

The waveguide with transformed metamaterial overlayer is shown on Fig. 3.4c without the object and together with it in Fig. 3.4d. Due to the effective material parameters obtained with the TO technique, the object does not scatter the incoming SPPs and an invisibility effect is demonstrated. Furthermore, the light flows smoothly around the object and the concealing effect is preserved for a wide range of refractive indices and materials, which agrees with the concepts of transformation optics.

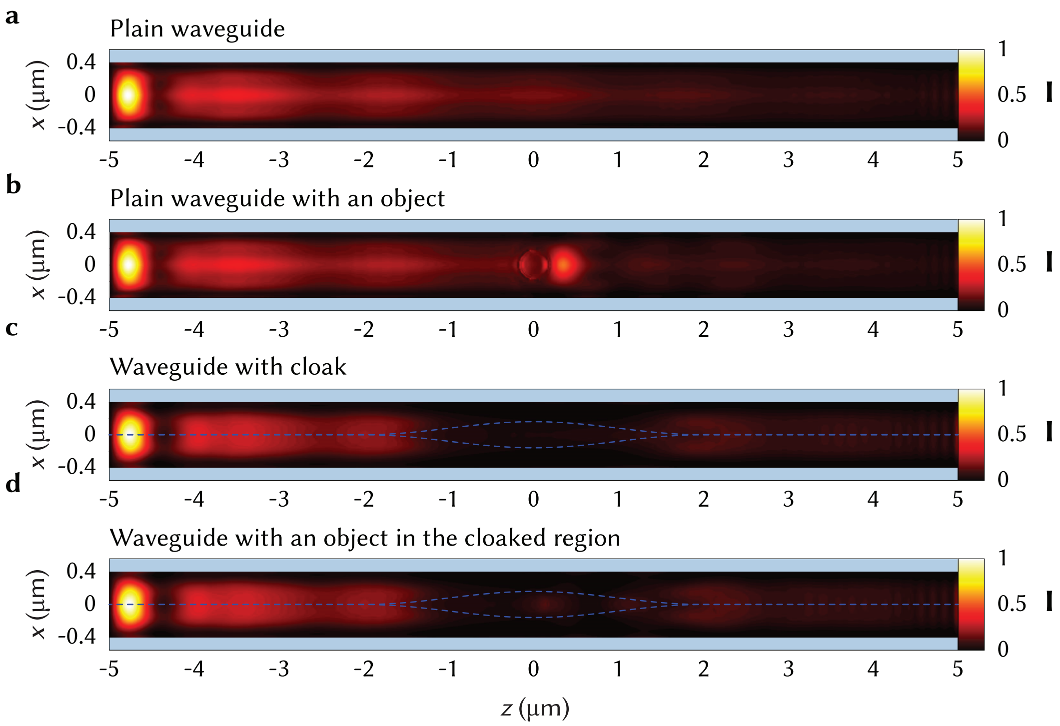

Figure 3.4 | Surface intensities of waveguide evanescent field cloak. **a**, Plain waveguide used for reference. **b**, Reference waveguide with cylindrical object placed on top. **c**, Waveguide with cloak. **d**, Waveguide with cloak an cylindrical object.

The current bottleneck of realization of an invisibility cloak is the implementation of the required parameters, especially at visible wavelengths. Furthermore, abrupt discontinuities in the material properties or geometries lead to increased scattering of SPPs, which significantly reduces the efficiency. Therefore, instead of directly modifying the RI of the dielectric medium, we propose to slowly change the thickness of an isotropic dielectric silicon overlayer, and hence the local effective index of SPPs [81]. In such a way, the propagation of SPPs can be controlled without directly modifying the metal surface or adding discrete scattering structures on the metal.

Fig. 3.5a plots the effective index of the HDM mode in our CPW as a function of the silicon overlayer thickness. The effective index increases with the thickness since more energy resides in the dielectric as shown in Fig. 3.5b, leading to stronger evanescent fields. The topology of the dielectric layer adjacent to a metal surface is linearly related to the calculated effective index in Fig. 3.3c. Furthermore, since the optical properties are changed gradually rather than abruptly, losses due to scattering can be significantly reduced.

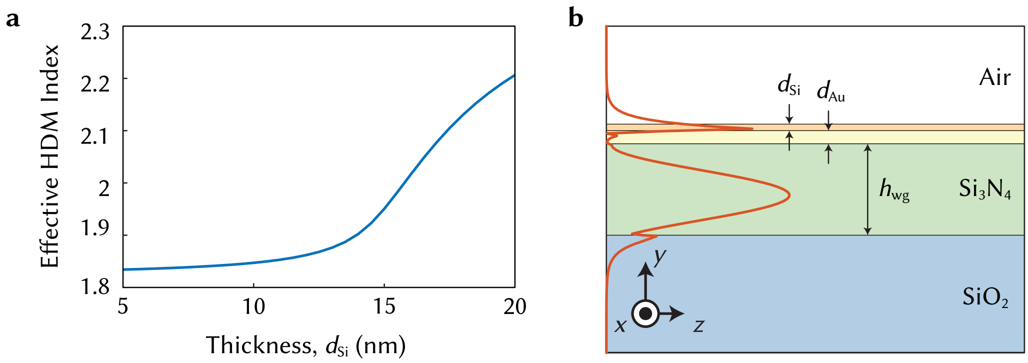

Figure 3.5 | Effective hybrid mode index as a function of dielectric layer thickness. **a**, The effective index of the HDM increases with silicon thickness due to more energy residing in the dielectric. **b**, Side view of the CPW geometry taken into consideration for the index calculations.

To summarize, we proposed and demonstrated an evanescent field cloaking scheme on composite plasmonic waveguide. The cloak design is based on the TO principles which allow to manipulate and distort the evanescent fields in a prescribed manner to conceal an object. A dielectric nano-spacer made of silicon is used to confine the light in vicinity with the metasurface boundary and facilitate the coupling to the hybrid plasmonic modes. The light manipulation is realized due to the engineered effective material parameters, which in turn suppresses the scattering effect. Our calculated results demonstrate that the designed metasurface can deflect the evanescent wave into a predefined, analytically calculated pattern. Since SPs are localized in the direction perpendicular to the metamaterial overlayer boundary and accompanied by the combination of the transverse and longitudinal electromagnetic fields, they have maximum intensity on the surface with the metamaterial overlayer. The gradient material properties of this layer allow the invisibility effect to take place. Our study of invisibility cloaking scheme with composite plasmonic waveguides and dielectric nano-spacer provides important insights to the complex behavior of hybrid plasmonic modes, on-chip light manipulation, and future design of integrated optical devices.

3.2 Silicon Waveguide Mode Converters

Photonic integrated circuits (PICs) based on silicon-on-insulator (SOI) technology hold great potential in various applications such as dispersion engineering [14, 82], on-chip information processing [83], chemical and biological sensors [84, 85], and photonic multiplexing systems [86, 87].

The speed of modern communication networks is limited by the heat generated from the on-chip electrical interconnects. Integration of photonic circuits on silicon to address the bandwidth bottleneck in on-chip data communications may provide a low-cost, scalable and efficient solution for the growing need of high data rates [88, 89].

Wavelength division multiplexing (WDM) is the most mature and common multiplexing technology widely used in telecommunications. However, WDM has limitations in bandwidth density scalability and requires multiple precise wavelength sources. The mode division multiplexing (MDM) offers an additional degree of freedom to scale communication bandwidth by utilizing separate guided modes to carry multiple data channels simultaneously using a single wavelength source. A key element in a MDM system is a mode converter that ideally can couple any given spatial mode into any other mode.

In this work, we take advantage of the discrete nature of waveguide modes [61] and the effective medium concept [90] to allow the design of ultra-compact and high-efficient mode conversion devices in a SOI platform. Furthermore, the proposed waveguide mode converter can be scaled to realize arbitrary waveguide mode conversion. As an example, we demonstrate two silicon waveguide mode converters employing all-dielectric metasurface structures that can convert the fundamental mode to higher order modes.

3.2.1 Silicon on Insulator Strip Waveguide

SOI strip waveguides are composed of high RI core made of Si on top of a lower RI SiO_2 buried oxide (BOX) confining light by reflections at the interface of the two materials on the basis of TIR. The structure in which we incorporate the mode converter waveguide is illustrated in Fig. 3.6a, with height h = 220 nm and width w = 1500 nm. This configuration can support up to three TE_j modes ($j = 0, 1, 2$) at the wavelength λ=1.55 µm. The numerically calculated electric field profiles of the the supported modes, $\left|E_x(x, y)\right|^2$, are shown in Figs. 3.6b-d, respectively. The modes have dominant electric fields in $\hat{x}$ direction while the $\hat{y}$ components are identical in the vertical direction (the waveguide has a single vertical mode).

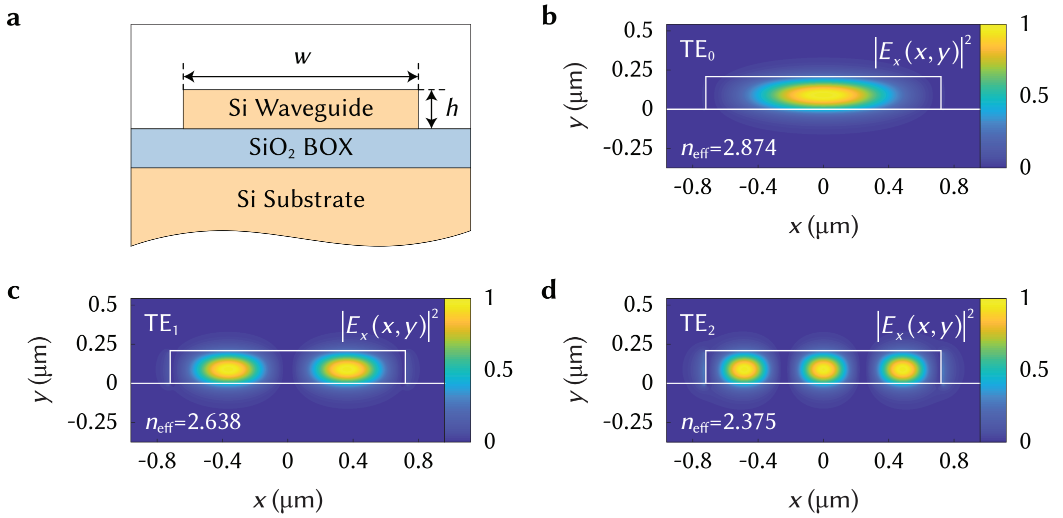

Figure 3.6 | Structure and calculated electric field profiles of the modes supported by the silicon strip waveguide.a, Schematic cross section of the waveguide structure. **b**, Fundamental TE_0 mode. **c**, TE_1 mode. **d**, TE_2 mode.

The height of the waveguide is the standard height of commercially available SOI wafers. The specific width is chosen in order to obtain a reasonable difference in the propagation constants β_j between the modes. A wider waveguide results in a nearly indistinguishable wavevectors and it will be nearly impossible to couple energy from one mode to another.

As seen from Eq. (2.11), the coupling coefficient is proportional to the spatial integration of the term $\mathbf{E}^*_m(x, y)\Delta\varepsilon^{(k)}(x, y, z)\mathbf{E}_n(x, y)$. We refer to this expression as the field overlap integral. Thus, in order to maximize the coupling coefficient and minimize the coupling length, several considerations must be taken in the choice of $\Delta\varepsilon(x, y, z)$. First, the phase matching in Eq. (2.12) should be satisfied by choosing the appropriate period Λ of the perturbation along propagation direction $\hat{z}$. Once phase matching had been established, proper choice of the the refractive index profile along the transverse direction is essential in order to achieve short coupling length.

3.2.2 Mode Converter Design and Numerical Validation

The proposed device is a co-directional coupler which couples two eigenmodes propagating along the same direction in a single multimode waveguide. We aim at converting the fundamental TE_0 mode to higher order $\mathrm{TE}_{1,2}$ modes. The dominant electric field components in the middle of the waveguide, $E_x(x, y = h/2)$, are shown in Fig. 3.7. The longitudinal components of the wavevectors of the modes govern the phase matching.

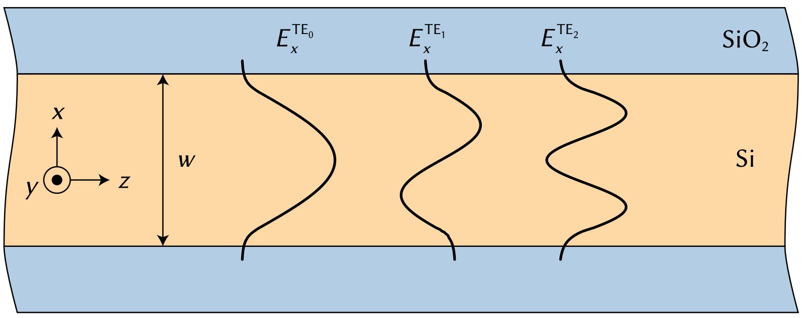

Figure 3.7 | Electric field profiles of the dominant component at the middle of the waveguide. The phase matching between the modes is governed by the longitudinal components of the wavevectors.

Since our multimode waveguide supports three TE_j modes, Eq. (2.10) reduces to a set three coupled equations. The amplitudes of propagation $A_j(z) = \psi_j e^{i\beta_j z}$ can be rewritten in terms of coupling coefficients and propagation constants

$$\begin{aligned}
\frac{d\psi_0}{dz} &= -i\left[\left(\beta_0 + \kappa_{00}\right)\psi_0 + \kappa_{01}\psi_1 + \kappa_{02}\psi_2\right] \\
\frac{d\psi_1}{dz} &= -i\left[\kappa_{10}\psi_1 + \left(\beta_1 + \kappa_{11}\right)\psi_1 + \kappa_{12}\psi_2\right] \\
\frac{d\psi_2}{dz} &= -i\left[\kappa_{20}\psi_0 + \kappa_{21}\psi_1 + \left(\beta_2 + \kappa_{22}\right)\psi_2\right]
\end{aligned} \tag{3.3}$$

where κ_{mn} is given by Eq. (2.11).

For efficient coupling, the dielectric perturbation must provide an effective wave vector k_{eff} in the opposite direction in order to compensate for the wavevector mismatch. When an incident waveguide mode propagates against k_{eff}, the bending angle of its wavevector increases, which corresponds to coupling from lower order into higher order waveguide modes. Coupling will occurs near the phase matching condition, i.e. $\beta_m - \beta_n - 2\pi k/\delta = 0$. For this to happen, the period should be chosen as to compensate for the β mismatch of the two modes. According to Eq. (2.11), for a constant perturbation, $\Delta\varepsilon^{(k)}$ will also be a constant and the coupling coefficient will vanish due to the orthogonality of the modes (see Eq. (2.6)). Therefore, $\Delta\varepsilon^{(k)}$ must vary along (x, y) in order to maximize the overlap integral in Eq. (2.10) by as much as needed so as to achieve a desired coupling length.

Similar to the formation of a hologram by the interference of two waves, we consider the interference of guided modes m and n in our design. Specifically, since we use the TE_0 mode as the input of the waveguide and we are interested in the interaction between the TE_0 and TE_i modes ($i = 1, 2$). We let the refractive index of the mode converter to vary in a sinusoidal fashion and take the real part such that

$$\begin{aligned}
\Delta\varepsilon(x, y, z) &= \varepsilon_0 n_{\text{Si}} \Delta n(x, y, z) \\
\Delta n(x, y, z) &= \mathrm{Re}\left[\Delta n(x, y) e^{i\left(\beta_m - \beta_n\right) z}\right]
\end{aligned} \tag{3.4}$$

where n_0 is the unperturbed part of the RI, $\Delta n(x, y, z)$ represents the periodic perturbation along the propagation direction $\hat{z}$. Expanding $\Delta n(x, y, z)$ into Fourier series provides the coefficients for a sinusoidal perturbation (i.e. $k = 1$ in Eq. (2.9)) so that $\Delta n^{(1)} = \Delta n(x, y)$. The cross-sectional RI profile is calculated using

$$\Delta n(x, y) = n_0 \left[E_x^{\mathrm{TE}_0}(x, y) \right]^* \left[E_x^{\mathrm{TE}_j}(x, y) \right], \quad i = 1, 2 \tag{3.5}$$

where n_0 is the amplitude of the index modulation and $E_x^{\mathrm{TE}_j}(x, y)$ are the unperturbed normalized electric field amplitude of the dominant $\hat{x}$ component for TE_0 and $\mathrm{TE}_{1,2}$ modes, respectively.

To further simplify the implementation of our proposed device, we do not use materials other than silicon for the core waveguide. Thus, the maximal value of $n(x, y, z)$ cannot exceed the refractive index n_{Si}. Furthermore, since the $\hat{y}$ components of the electric fields are identical in the vertical direction, $n(x, y, z)$ is uniform along the y axis and index variation is only applied along along the horizontal x axis in order to control the overlap between the field of the two modes. These features make the fabrication of our proposed device much simpler.

In order to validate our design, we numerically simulated the two cases of mode converter devices, $\mathrm{TE}_0 \rightarrow \mathrm{TE}_1$ and $\mathrm{TE}_0 \rightarrow \mathrm{TE}_2$, to obtain the 3D electromagnetic fields. In order to quantify the device performance, we have lunched the TE_0 mode to the input waveguide and decomposed the computed fields at the output on the basis of the waveguide eigenmodes [48]. This allowed us to determine the power transmission of each mode through the device and compute the mode purity and the total transmission efficiency of the device.

The schematic of the studied system is shown in Fig. 3.8a where the TE_0 mode at the input shown in Fig. 3.8b is converted to the TE_1 mode at the output in Fig. 3.8c. The calculated sinusoidal index perturbation in both the longitudinal and transverse directions with length L is shown in Fig. 3.8d causes energy to gradually couple out of the input mode and into the output mode as demonstrated by the mode field evolution in Fig. 3.8e. We decomposed the output fields to find the conversion efficiency between the mode of 95.4% over length $L = 8.91$ µm with modulation index $c_0 = 0.2$.

Similarly to the results presented above, Fig. 3.9 shows design and calculated results of a TE_0 to TE_2 converter over the same waveguide geometry. The structure in Fig. 3.9a is excited with the TE_0 mode in Fig. 3.9b and gradually coupled into

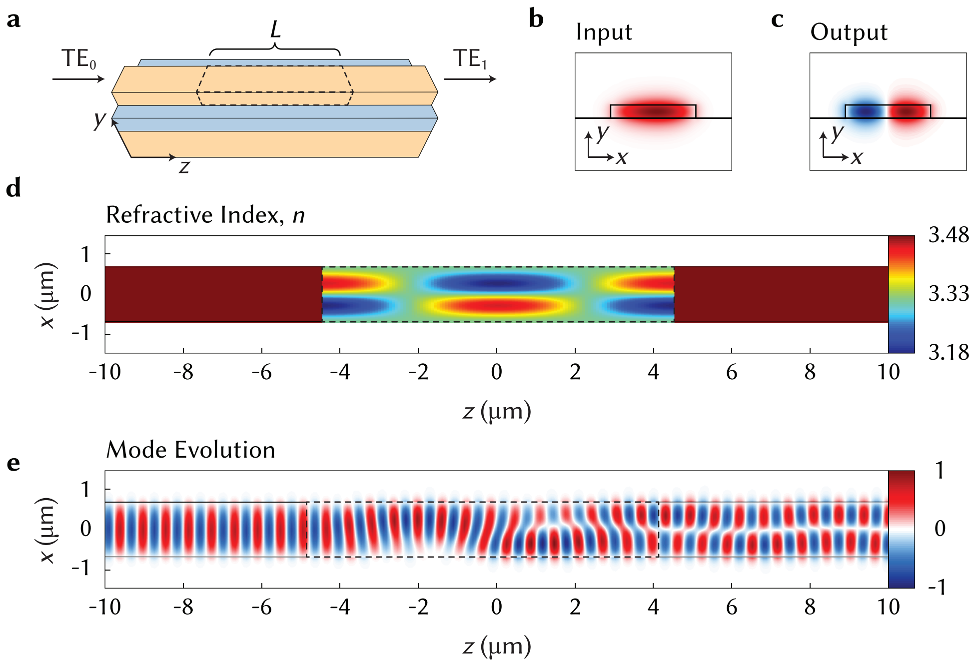

Figure 3.8 | Waveguide TE_0-to-TE_1 mode converter with sinusoidal index perturbation. **a**, Structure of the studied waveguide mode converter configuration. **b**, Electric field profile of the input TE_0 mode. **c**, Electric field profile of the output. **d**, Refractive index profile of the device. The right and left uniform sections represent the input and output waveguides, and the intermediate segment between them is the converter section with length L. **e**, Mode evolution $E_x(x, y = h/2, z)$ as light propagates from left to right.

the TE_2 mode at the output shown in Fig. 3.9c. The calculated sinusoidal index profile in Fig. 3.9c is responsible for the gradual conversion into the output mode as shown in Fig. 3.9d. This device achieves conversion efficiency of 96.4% over length L = 6.32 µm and modulation index of c_0 = 0.31.

As expected, the FDTD simulations shows a behavior of power exchange between the modes, and the results are in good agreement with the analytic calculations. Next, we discuss the practical implementation of the proposed device.

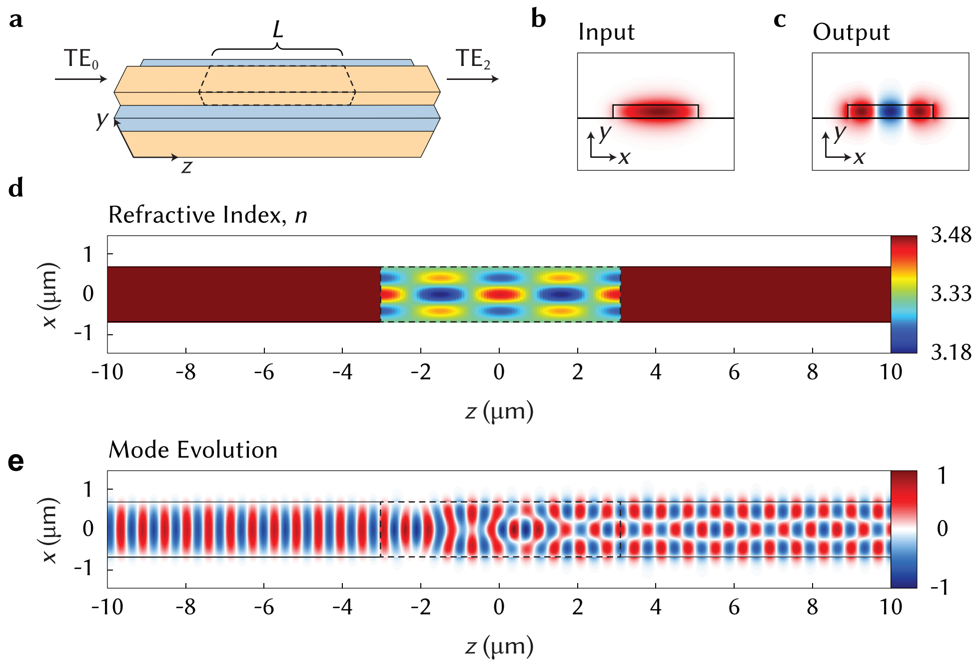

Figure 3.9 | Waveguide TE_0-to-TE_2 mode converter with sinusoidal index perturbation. **a**, Structure of the studied waveguide mode converter configuration. **b**, Electric field profile of the input TE_0 mode. **c**, Electric field profile of the output. **d**, Refractive index profile of the device. The right and left uniform sections represent the input and output waveguides, and the intermediate segment between them is the converter section with length L. **e**, Mode evolution $E_x(x, y = h/2, z)$ as light propagates from left to right.

3.2.3 Implementation of a Real Device

In the previous examples, we demonstrated ”ideal” devices based on a continuous sinusoidal perturbation. However, implementing a sinusoidally changing refractive index over a large index span is very challenging in practice. After presenting the basic concepts of the proposed device we can now turn to discuss the practical considerations and guidelines for determining the parameters of a real device.

Our proposed device is based on all-dielectric metasurface structure with a tilted subwavelength periodic perturbation. By utilizing the diagonal symmetry of the calculated RI profiles, we design the physical structure which emulates it using the effective medium approach [76].

The schematics of our proposed mode converter are shown in Fig. 3.10. Fig. 3.10a depicts the 3D structure of our waveguide mode converter where N tilted corrugations with duty cycle f are etched into the Si core of the waveguide forming a dielectric metasurface with length L. The top view of the metasurface is shown in Fig. 3.10b with the titled periodic corrugations with period δ and angle θ. The transverse cross section of the waveguide is shown in Fig. 3.10c with the corrugation depth t, the waveguide height h = 220 nm and width w = 1500 nm. The cross sections at point I, II and III are shown in Fig. 3.10d, respectively.

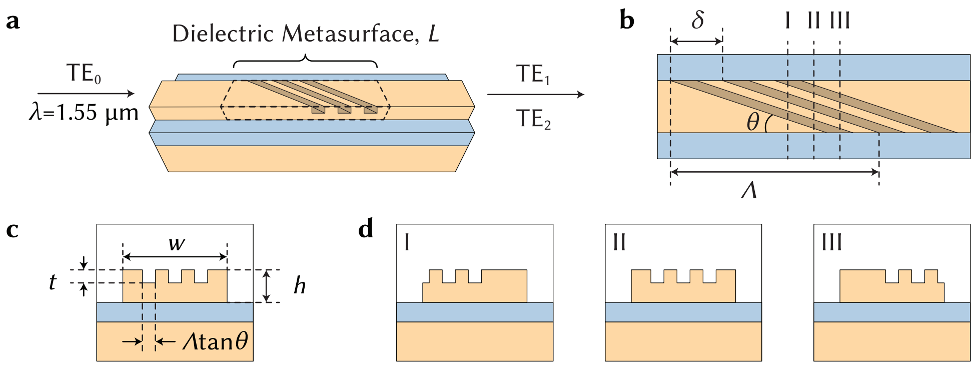

Figure 3.10 | Schematic of the proposed waveguide mode converter. **a** 3D Schematic of the proposed mode converter waveguide based on tilted periodic perturbations. **b**.

As previously mentioned, $n(x, y, z)$ should be smaller than n_{Si} in order not to exceed RI. Still, there are additional considerations which one needs to take into account. On the one hand, larger values of index modulation will maximize the coupling coefficient and thus provide shorter coupling length and makes the device less sensitive to β mismatch. On the other hand, these parameters affect the minimal subwavelength feature size and one should choose their combination taking into account fabrication constraints. Moreover, lower values of $n(x, y, z)$ will increase Fresnel reflections and losses in the mode converter due to the index mismatch.

The specific parameters required for each mode converter are calculated as follows. We initially calculate numerically the EM fields of the TE modes (see Fig. 3.6).

Next, the length of a single corrugation is set to Λ based on the phase matching condition in Eq. (2.12) and the angle θ using

$$\theta = \arctan\left[\frac{2w}{(j+1)\Lambda}\right] \tag{3.6}$$

where j is the mode number we aim to convert from the fundamental mode (i.e $j = 1, 2$). We use the effective index method (EIM) to provide the initial guess for the amount of corrugations N, their period δ and duty cycle f. Their exact values are optimized and set based on numerical simulations. We found that setting the corrugation etch depth to $t = 100$ nm provides the best trade-off between device dimensions and performance.

The proposed structure provides a sinusoidally changing coupling coefficient κ_{0j} along the propagation direction $\hat{z}$. In the transverse direction $\hat{x}$, the gradual change of κ_{0j} makes it $\hat{z}$ dependent to ensure constructive contribution to the conversion.

3.2.4 Waveguide Mode Conversion

A FDTD simulator was used to obtain the 3D electromagnetic fields in the mode converter with all-dielectric metasurface structure based on tilted subwavelength periodic perturbations. The specific parameters required for each mode converter were obtained and optimized using numerical simulations. The optimization is required to fine tune the phase matching condition for optimal performance.

The corresponding structures and electric field profiles of the mode converters are shown in Fig. 3.11. Fig. 3.11a shows the top view of the structure of the proposed $TE_0 \longrightarrow TE_1$ mode converter. Tilted subwavelength periodic perturbations with parallelogram shapes are etched on a silicon waveguide to form dielectric metasurface structures. The numerically calculated electric field distribution at the middle of the waveguide, $E_x(x, y = h/2, z)$, is shown in Fig. 3.11b. The input TE_0 mode launched from the left is gradually converted into the output TE_1 mode over length L. The scalability of our proposed metasurface structure is further demonstrated by the $TE_0 \longrightarrow TE_2$ mode converter. Fig. 3.11c shows top view of the structure and Fig. 3.11d shows the calculated electric field distribution of the proposed device.

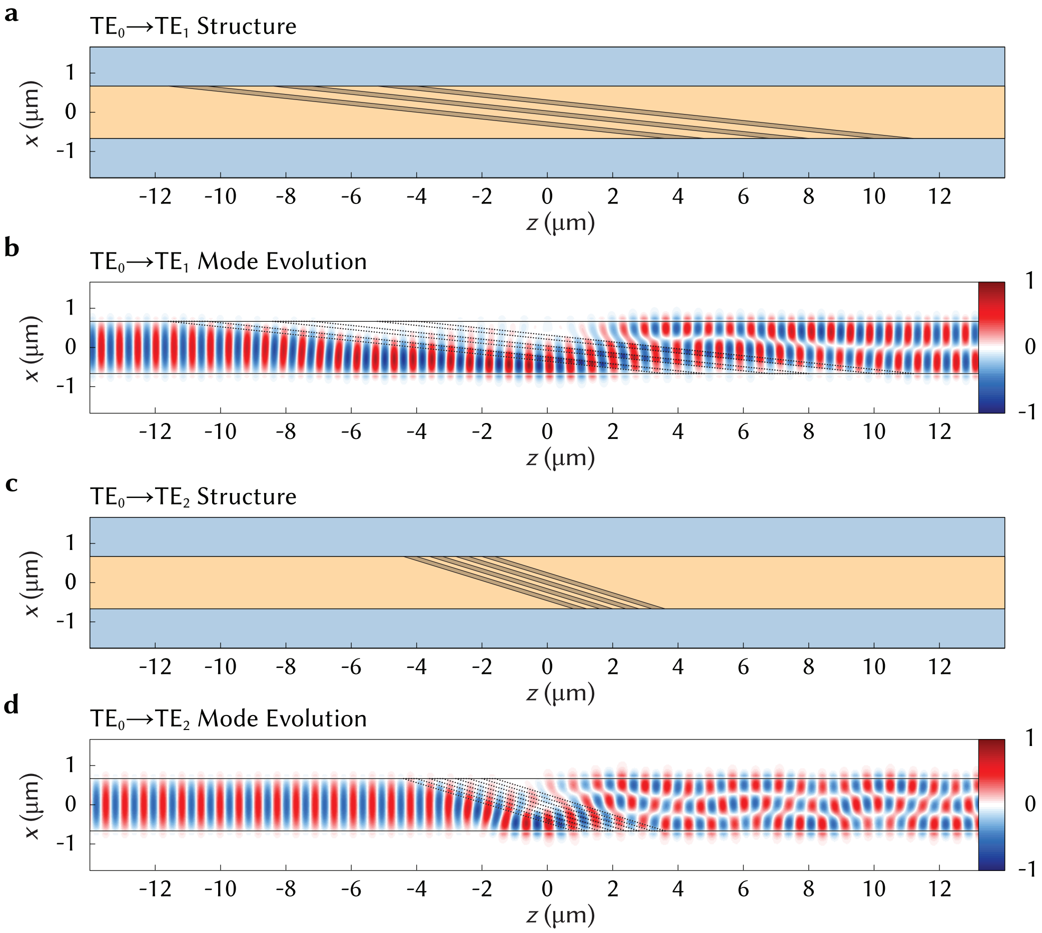

Figure 3.11 | Waveguide mode converters with tilted subwavelength periodic perturbations. **a**, Structure of the $TE_0 \longrightarrow TE_1$ converter. **b**, Electric field profile showing the power exchange between the modes along the propagation. **c**, Structure of the $TE_0 \longrightarrow TE_2$ converter. **b**, Electric field profile showing the power exchange between the modes along the propagation.

The specific design parameters and performance of the mode converters are summarized in Table 3.1.

To evaluate the spectral behavior of the waveguide mode converters, we decomposed the output fields on the basis of the waveguide eigenmodes and computed the output power transmission of each mode. Fig. 3.12 shows the mode converters

Table 3.1: Design parameters of the waveguide mode converters.

Mode Converter	Length, L (µm)	Angle, θ (deg)	Period, Λ (µm)	Periods	Duty Cycle, f (%)	Conversion Efficiency (%)
$TE_0 \rightarrow TE_1$	19.6	5.4	3	3	50	96
$TE_0 \rightarrow TE_2$	5.2	14.8	0.75	4	35	92

transmission and modal crosstalk as a function of wavelength in the C-band (conventional band, 1530-1565 nm) range commonly used for optical communication.

In Fig. 3.12a, the modal crosstalk of the output TE_1 with the input TE_0 modes reaches minimal value at the designated operation wavelength of λ = 1.55 µm. At this wavelength, the energy exchange between the input and output modes is maximal while the higher order TE_2 mode is suppressed. The modal transmission of the $TE_0 \rightarrow TE_2$ mode converter is shown Fig. 3.12b. The spectral behavior resembles that of the $TE_0 \rightarrow TE_1$ converter. Consequently, the TE_2 mode power peaks at λ = 1.55 µm while the power of input TE_0 mode is minimal and the TE_1 mode is completely suppressed.

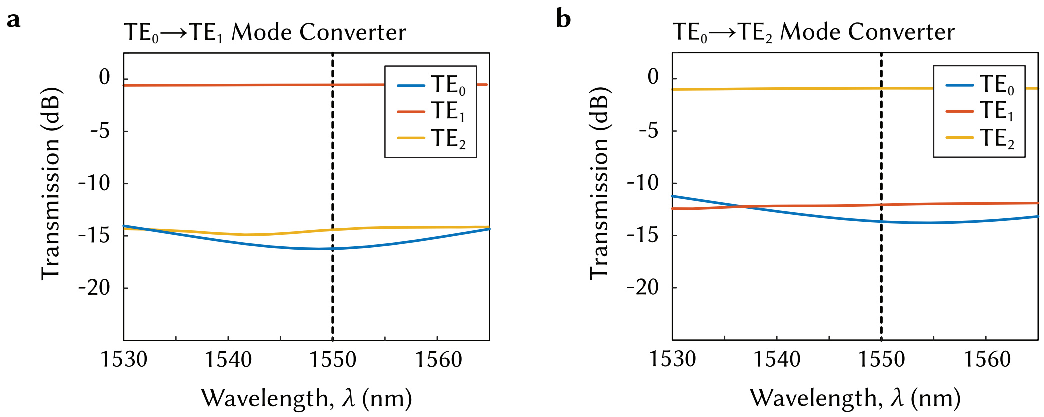

Figure 3.12 | Transmission and modal crosstalk of the waveguide mode converters. **a**, Output power of the supported TE modes in the $TE_0 \rightarrow TE_1$ mode converter. **b**, Output power of the supported TE modes in the $TE_0 \rightarrow TE_2$ mode converter.

To summarize, we have proposed and demonstrated a compact silicon waveguide mode converter implemented with tilted dielectric metasurface structure. The metasurface provides a sinusoidally changing coupling coefficient that changes along the propagation and allows mode conversion on the same waveguide. We presented the semi-analytical design procedure and validated it using numerical simulations. Two silicon waveguide mode converters employing all-dielectric metasurface structures were numerically demonstrated. Our proposed waveguide mode converters can be scaled to realize arbitrary waveguide mode conversions. The demonstrated coupling and conversion of waveguide modes provide a general method to manipulate on-chip optical modes, and may find applications in integrated mode-division communication and optical signal processing systems.

3.3 Nearly Guided Wave Surface Plasmon Resonance Sensor

The development of SPR sensors for detecting molecular interactions is of great importance for chemical and biological sensing due to its distinctive features such as high sensitivity, label-free measurement, and real-time analysis. To excite the SPs, Kretschmann configuration based on attenuated total reflection is generally used. In a conventional SPR biosensor based on this configuration, a thin film of metal is deposited on the base of a high index prism, and a sensing medium is kept in contact with the metal film. When the momentum of the incident light on the structure matches with that of the SPs, a sharp resonant dip in the reflection response can be observed.

The sensitivity, which is defined as the ratio of the shift in the resonance angle θ_r or wavelength λ_r in the angular interrogation mode or spectral interrogation mode, respectively, to the change in the RI of the sensing medium n_s, is given by

$$S_\theta = \frac{\Delta\theta_r}{\Delta n_s}\,, \quad S_\lambda = \frac{\Delta\lambda_r}{\Delta n_s} \tag{3.7}$$

To achieve a high sensitivity, both the absorption efficiency and the sensitivity to RI change must be high. However, molecules generally exhibit poor absorption on a metal surface in a conventional SPR biosensor.

3.3.1 Nearly Guided Wave SPR

The introduction of an additional dielectric film layer between the metal and the sensing medium can provide a way for sensitivity improvement in the so called nearly guided wave surface plasmon resonance (NGWSPR) sensor, which is similar to the Kretschmann configuration with an addition of a thin dielectric film between the metal layer and the sample as shown in Fig. 3.13a.

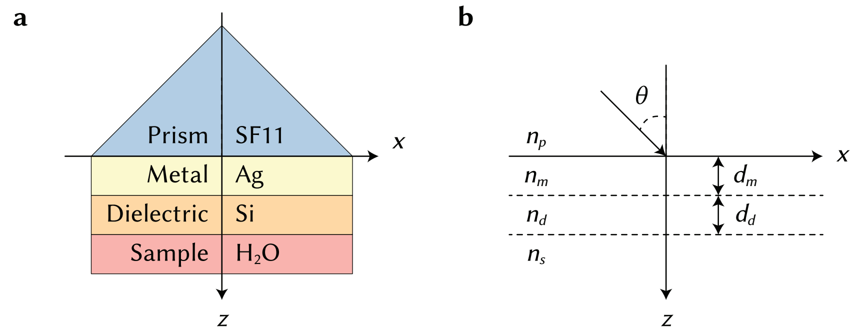

Figure 3.13 | Schematic diagram and model of NGWSPR sensor. a, The NGWSPR sensor has an additional dielectric film layer between the metal and the sensing medium. **b**, Multilayer model of the NGWSPR sensor used for calculations.

The performance of the NGWSPR sensor structure is analyzed using typical thin-film theory based on the schematic in Fig. 3.13b. For this structure, each layer is represented by its characteristic matrix given by Eq. (2.2) and the total reflection response is obtained by cascading the matrices for the thin layers using Eq. (2.3).

The structure in Fig. 3.13 is composed of a N-SF11 glass prism coated with silver film of thickness d_m = 47 nm, silicon film of thickness d_d = 10 nm and we use water (H_2O) as our sensing medium. The thickness of the film was optimized using numerical simulations while taking in account the 2 nm native oxide layer (SiO_2) on top of the silicon. This configuration allows to improve the absorption efficiency of the sensing medium as well as exploring SPR in the near infrared (NIR) spectrum.

3.3.2 Experiment

The structure was manufactured using standard electron beam chemical vapor deposition (EPCVD) process. The thin films of silver and silicon were deposited on a planar glass substrate of the same material of the prism and we used index matching fluid for our experiment between the manufactured structure and the prism. We preformed profilometer to examine the surface profile of the device and found the manufactured silver thickness to be $d_m = 52$ nm and used this value for our calculations.

The schematic diagram of the experimental setup for NGWSPR is shown in Fig. 3.14. We use a fiberized broadband light as the source in our setup (Thorlabs SLS201L), which allows simultaneous angular and wavelength interrogation. The source is connected to a reflective collimator (Thorlabs RC04) by an optical fiber. This type of achromatic collimator provides stable focus over a wide range of wavelengths. The collimated light passes through a polarizer (Thorlabs WP25M-UB) to achieve TM polarization and is incident upon the prism. The reflected light is collimated onto a fiber facet using an objective (Olympus RMS4X) and the spectral reflectance is captured using an optical spectrum analyzer (Yokogawa AQ6370B). For accurate and full representation of the system, we define the angle φ as the incident angle upon the prism from the air side. It is related to the internal angle θ by $\varphi = \arcsin\left[n_p \sin(\theta - \pi/4)\right]$.

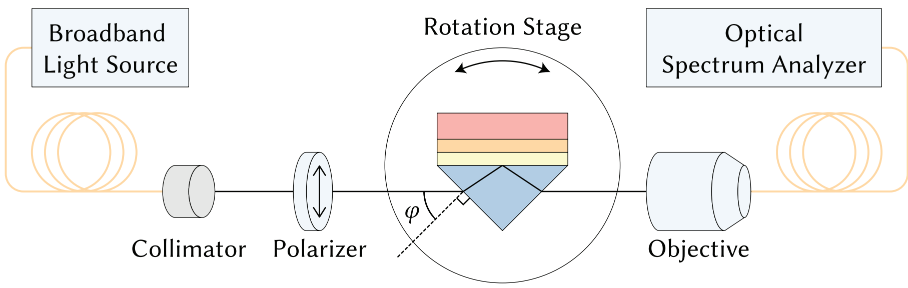

Figure 3.14 | Schematic diagram of the experimental setup for NGWSPR sensor. Polychromatic light is collimated, polarized and incident upon the structure. The reflected light is collected with an objective and measured using a spectrum analyzer.

The experimentally obtained output normalized reflectance spectra for several values of φ are shown in Fig. 3.15 along with the theoretical curves. The results show good correspondence with the theoretically computed values with a total relative error of 3.7 %. With relatively small changes of the incident angle upon the prism φ, the resonance experiences an abruptly shift which increases with λ, indicating that the sensitivity increases with the wavelength. The calculated sensitivity of the NGWSPR sensor reaches 170 deg/RIU which is 50% increase compared to the same sensor without the additional optimized dielectric layer.

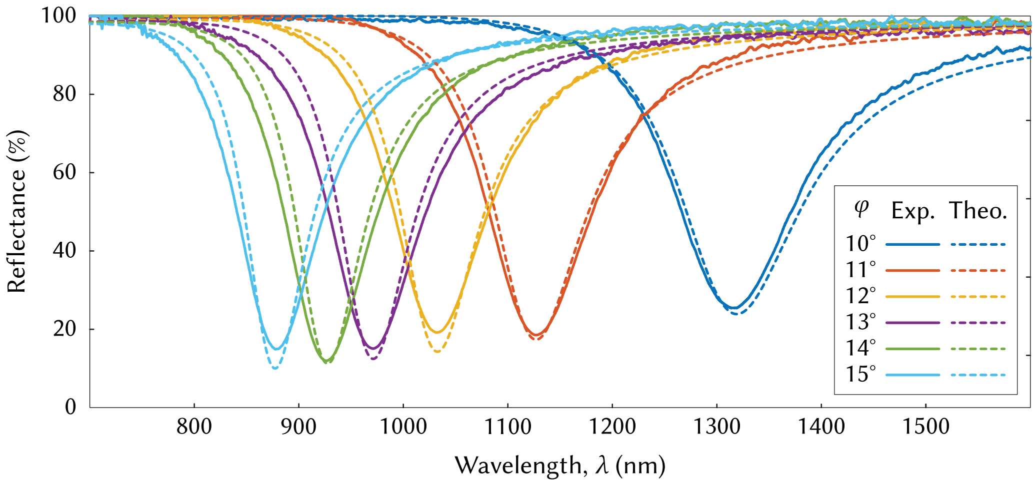

Figure 3.15 | Experimental results of NGWSPR sensor. Calculated and experimentally obtained reflection responses as a function of wavelength for several incident angles. The experimental results correspond with calculated theoretical values.

Fig. 3.16 show the dispersion map of the NGWSPR sensor as a function of angle φ and wavelength λ. While the increased sensitivity is mainly attributed to the optimized dielectric thickness, the absorption efficiency is mainly determined by the metal. On the one hand, with increasing values of λ, the metal exhibits higher losses which leads to more absorbed photons. On the other hand, the momentum of photons with longer λ is lower, which is easier to match, resulting in SPs excited at a broader spectral and angular ranges. Consequently, these mechanism cause the minimal values and bandwidth of each resonance to increase and expand, respectively.

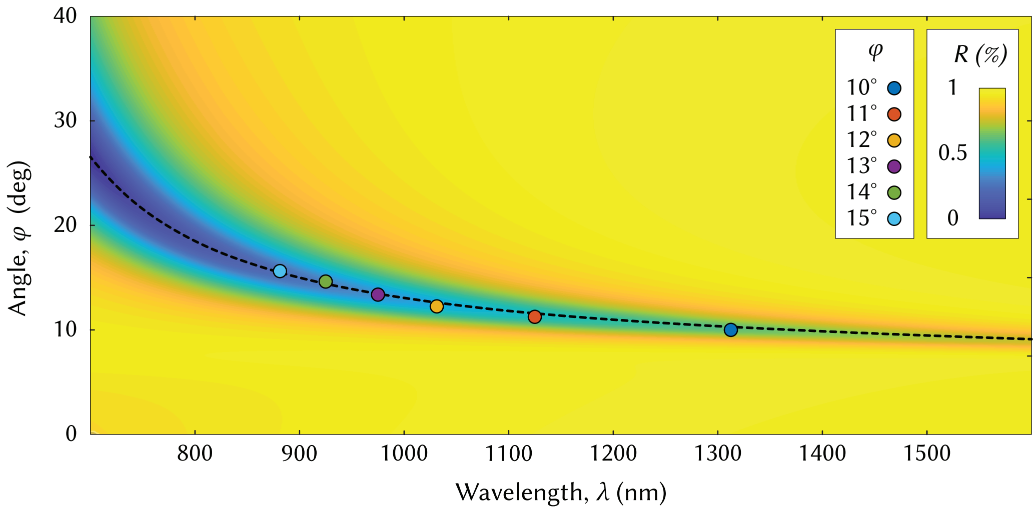

Figure 3.16 | Dispersion map of NGWSPR sensor. Calculated reflection response as a function of wavelength and incident angles with experimental results indicated on the map.

To summarize, the NGWSPR sensor has been theoretically investigated and experimentally demonstrated. An additional dielectric silicon film thickness was introduced between the metal and the sample compared to typical SPR configuration in order to increase the absorption efficiency and performance of the device. The dielectric thickness was optimized for enhanced sensitivity. The device was manufactured and the experiments show good agreement with the theoretically calculated results using conventional thin film theory. We discussed various parameters affecting the sensitivity and absorption efficiency of the device which we took under consideration in the design process.

The simultaneous angular and wavelength interrogation provides important insights to the various parameters affecting SPR sensors. Good sensing characteristics were obtained with a simple device structure. Further improvements of SPR sensors characteristics is of great interest for various applications and offers great opportunities for high-level integration of SPR sensors.

3.4 Anti-reflective Subwavelength Structures for Waveguide Facets

For many waveguide devices, facet reflectivity is a design parameter of fundamental importance. In particular, the Fresnel reflectivity of waveguide facets often needs to be reduced to ensure functionality and to improve performance of devices.

For high-index-contrast passive devices, such as silicon waveguides, the Fresnel reflection at the facet is a significant contributor to the fiber-to-chip coupling loss and the return loss. Currently, the common method to reduce facet reflectivity of planar waveguides is the deposition of anti-reflection (AR) coatings on the facets [91, 92]. Here, we present the use of subwavelength structures for facet reflectivity reduction by the GRIN effect.

3.4.1 Design and Numerical Model

Our design is based on Si rib waveguide with conical structures etched into the facet. Since diffraction effects are frustrated due to the subwavelength nature, the light passing from the waveguide to freespace is affected primarily by the effective average index of the structure. This arrangement acts as an AR GRIN layer which is less wavelength sensitive than AR coatings.

The schematic of the system we used for our numerical simulations is illustrated in Fig. 3.17a. In order to achieve good representation of an actual butt-coupled waveguide, we used a Gaussian beam with parameters representing a standard SMF28 fiber. The two dimensional view of the facet is shown Fig. 3.17b, the structures are mapped in an hexagonal arrangement in order to maximize the fill factor. The waveguide is of a rib type geometry, where the rib width is $W = 10$ µm, height $h = 0.5$ µm and slab height of $H = 1.9$ µm.

In order to determine the optimal gradient structure, we preformed simulations with different cone geometries shown in in Fig. 3.17c: parabolic, rounded tip and truncated cones, respectively. Based on preliminary simulations, we chose cone base diameter of $d_b = 550$ nm and cone height of $h_c = 900$ nm. These values allow maximal filling of the facet and are applicable for fabrication.

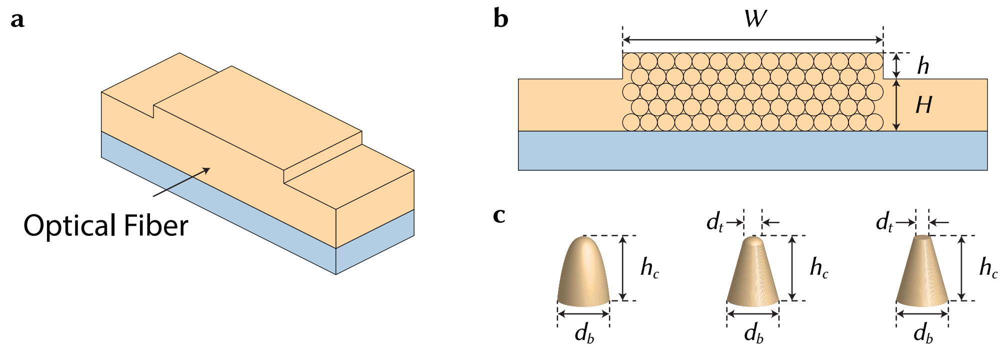

Figure 3.17 | Schematic of the proposed waveguide facet anti-reflective structure. **a**, A Gaussian beam representing an SMF28 fiber is butt-coupled with a rib waveguide. **b**, 2D view of waveguide facet with the hexagonal mapping of the subwavelength structures. **c**, Geometry of the structures used as a unit cell.

3.4.2 Simulation Results

As previously stated, the simulations consist of a numerical model which represents the actual experimental situation, where a Gaussian beam emitted from a fiber is incident upon the waveguide facet. To measure the transmittance, we integrate the power inside the waveguide, and the reflectance is measured by integrating the power flow in the backward direction outside the waveguide and removing the incident field.

The reflectance of the structure is shown in Fig. 3.18a. While the reflectance of a reference waveguide with a plain facet averages at 13%, the reflectance of a waveguide with the AR structure exhibit values below 2% with minimal avarage value of 1.49% achieved with the parabolic cones. The transmittance is show in in Fig. 3.18b, similarly to the reflectance, the structured facet allows more energy to couple into the waveguide with maximal average value of 98.13% using the parabolic cones.

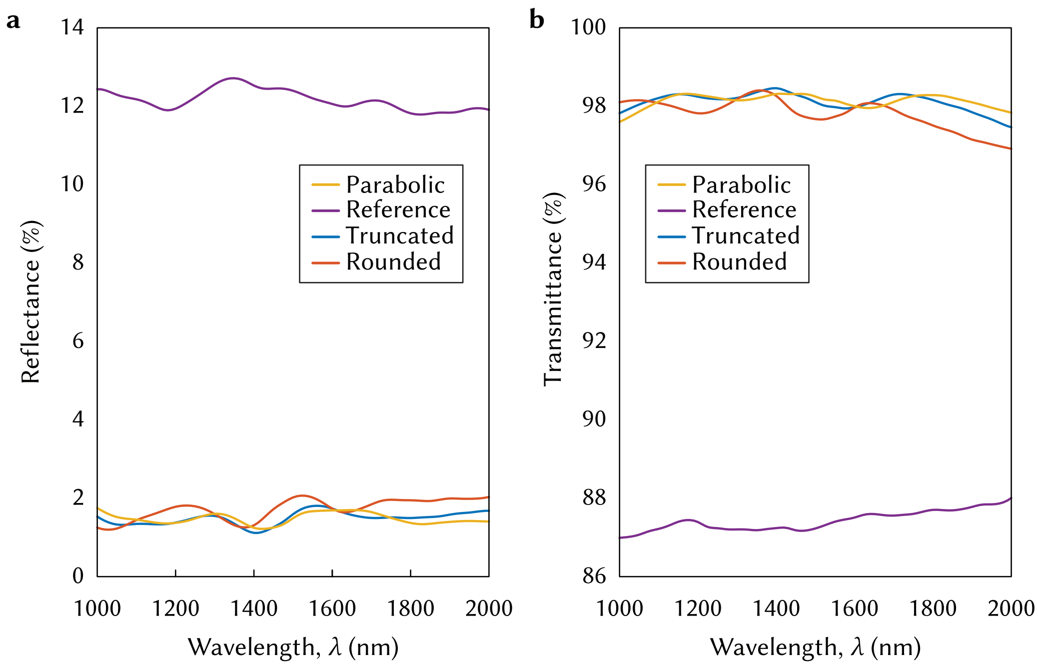

Figure 3.18 | Calculated reflectance and transmittance of a waveguide with anti-reflective structure on its facet. **a**, Reflectance. **b**, Transmittance. The parabolic cones exhibit the best performance characteristics.

4 Conclusion

In this thesis, we have studied the phenomena associated with subwavelength structured materials on optical waveguides and surface plasmon sensors. We presented the theory and the mandatory fundamental concepts we applied in our work. Three types of implementations for optical devices operating in the subwavelength regime were demonstrated, and in each section, we presented the design and results of optical devices utilizing complex materials for enhanced functionality and novel optical phenomena including evanescent field waveguide cloak, compact silicon waveguide mode converter, enhanced sensitivity SPR sensor, and anti-reflective structures for waveguide facets.

The major contributions of this research include:

- Evanescent field waveguide cloaking. A composite plasmonic waveguide based electromagnetic cloaking scheme has been proposed and demonstrated. We have shown that by manipulating the effective index of a dielectric nanospacer, the scattering fields of an object located on the cloak do not interact with the evanescent field, resulting in an invisibility effect.

- Silicon waveguide mode converters. We explored the discrete nature of waveguide modes and the effective medium concept to achieve a simple, yet compact and efficient waveguide mode conversion device. The modes are converted on the same waveguide and similar concept can be applied to realize arbitrary waveguide mode conversions.

- Enhanced performance SPR sensor. We have shown that the sensitivity of transitional SPR sensors can be enhanced by 50% with an additional dielectric film between the metal and the sample. The film thicknesses were optimized for optimal performance and experimental results have shown good agreement with our calculations.

- Anti-reflective structures for waveguide facets. We demonstrated by numerical simulations that the facet transmittance of a ridge waveguide can reached 98% with subwavelength structures parabolic cones are etched onto it.

References

[1] M. J. Weber. *Handbook of Optical Materials.* CRC press, 2018.

[2] M. Born and E. Wolf. *Principles of Optics: Electromagnetic Theory of Propagation, Interference and Diffraction of Light.* Elsevier, 2013.

[3] A. M. Urbas, Z. Jacob, L. Dal Negro, N. Engheta, A. Boardman, P. Egan, A. B. Khanikaev, V. Menon, M. Ferrera, N. Kinsey, et al. "Roadmap on Optical Metamaterials". *Journal of Optics* 18:9, 2016, p. 093005.

[4] Y. Xu, Y. Fu, and H. Chen. "Planar Gradient Metamaterials". *Nature Reviews Materials* 1:12, 2016, p. 16067.

[5] W. C. Chew, E. Michielssen, J. Song, and J.-M. Jin. *Fast and Efficient Algorithms in Computational Electromagnetics.* Artech House, Inc., 2001.

[6] W. L. Barnes, A. Dereux, and T. W. Ebbesen. "Surface Plasmon Subwavelength Optics". *nature* 424:6950, 2003, p. 824.

[7] D. K. Gramotnev and S. I. Bozhevolnyi. "Plasmonics Beyond the Diffraction Limit". *Nature photonics* 4:2, 2010, p. 83.

[8] S. Jahani and Z. Jacob. "All-dielectric Metamaterials". *Nature nanotechnology* 11:1, 2016, p. 23.

[9] N. Yu, P. Genevet, M. A. Kats, F. Aieta, J.-P. Tetienne, F. Capasso, and Z. Gaburro. "Light Propagation with Phase Discontinuities: Generalized Laws of Reflection and Refraction". *science* 334:6054, 2011, pp. 333–337.

[10] Q. Wang, E. T. Rogers, B. Gholipour, C.-M. Wang, G. Yuan, J. Teng, and N. I. Zheludev. "Optically Reconfigurable Metasurfaces and Photonic Devices based on Phase Change Materials". *Nature Photonics* 10:1, 2016, p. 60.

[11] A. V. Kildishev, A. Boltasseva, and V. M. Shalaev. "Planar Photonics with Metasurfaces". *Science* 339:6125, 2013, p. 1232009.

[12] N. Yu and F. Capasso. "Flat Optics with Designer Metasurfaces". *Nature materials* 13:2, 2014, p. 139.

[13] N. Engheta and R. W. Ziolkowski. *Metamaterials: Physics and Engineering Explorations*. John Wiley & Sons, 2006.

[14] Y. Galutin, E. Falek, and A. Karabchevsky. "Invisibility Cloaking Scheme by Evanescent Fields Distortion on Composite Plasmonic Waveguides with Si Nano-Spacer". *Scientific reports* 7:1, 2017, p. 12076.

[15] Y. Greenberg and A. Karabchevsky. "Spatial Eigenmodes Conversion with Metasurfaces Engraved in Silicon Ridge Waveguides". *Applied Optics* 58:22, 2019, F21–F25.

[16] D. Schurig, J. Mock, B. Justice, S. A. Cummer, J. B. Pendry, A. Starr, and D. Smith. "Metamaterial electromagnetic cloak at microwave frequencies". *Science* 314:5801, 2006, pp. 977–980.

[17] T. Ergin, N. Stenger, P. Brenner, J. B. Pendry, and M. Wegener. "Three-Dimensional Invisibility Cloak at Optical Wavelengths". *science* 328:5976, 2010, pp. 337–339.

[18] X. Ni, Z. J. Wong, M. Mrejen, Y. Wang, and X. Zhang. "An Ultrathin Invisibility Skin Cloak for Visible Light". *Science* 349:6254, 2015, pp. 1310–1314.

[19] Z. Jacob, L. V. Alekseyev, and E. Narimanov. "Optical hyperlens: far-field imaging beyond the diffraction limit". *Optics express* 14:18, 2006, pp. 8247–8256.

[20] X. Zhang and Z. Liu. "Superlenses to overcome the diffraction limit". *Nature materials* 7:6, 2008, p. 435.

[21] J. B. Pendry. "Negative Refraction Makes a Perfect Lens". *Physical review letters* 85:18, 2000, p. 3966.

[22] R. A. Shelby, D. R. Smith, and S. Schultz. "Experimental Verification of a Negative Index of Refraction". *science* 292:5514, 2001, pp. 77–79.

[23] J. Pendry. "A Chiral Route to Negative Refraction". *Science* 306:5700, 2004, pp. 1353–1355.

[24] V. M. Shalaev, W. Cai, U. K. Chettiar, H.-K. Yuan, A. K. Sarychev, V. P. Drachev, and A. V. Kildishev. "Negative Index of Refraction in Optical Metamaterials". *Optics letters* 30:24, 2005, pp. 3356–3358.

[25] A. Y. Piggott, J. Lu, K. G. Lagoudakis, J. Petykiewicz, T. M. Babinec, and J. Vučković. "Inverse Design and Demonstration of a Compact and Broadband On-Chip Wavelength Demultiplexer". *Nature Photonics* 9:6, 2015, p. 374.

[26] Z. Li, M.-H. Kim, C. Wang, Z. Han, S. Shrestha, A. C. Overvig, M. Lu, A. Stein, A. M. Agarwal, M. Lončar, et al. "Controlling Propagation and Coupling of Waveguide Modes Using Phase-Gradient Metasurfaces". *Nature nanotechnology* 12:7, 2017, p. 675.

[27] P. Cheben, R. Halir, J. H. Schmid, H. A. Atwater, and D. R. Smith. "Subwavelength Integrated Photonics". *Nature* 560:7720, 2018, p. 565.

[28] B. Shen, P. Wang, R. Polson, and R. Menon. "An Integrated-Nanophotonics Polarization Beamsplitter with 2.4× 2.4 μm 2 footprint". *Nature Photonics* 9:6, 2015, p. 378.

[29] R. H. Ritchie. "Plasma Losses by Fast Electrons in Thin Films". *Physical review* 106:5, 1957, p. 874.

[30] B. Hecht, H. Bielefeldt, L. Novotny, Y. Inouye, and D. Pohl. "Local Excitation, Scattering, and Interference of Surface Slasmons". *Physical review letters* 77:9, 1996, p. 1889.

[31] H. Raether. "Surface Plasmons on Smooth Surfaces". In: *Surface plasmons on smooth and rough surfaces and on gratings.* Springer, 1988, pp. 4–39.

[32] J. Zhang, L. Zhang, and W. Xu. "Surface Plasmon Polaritons: Physics and Applications". *Journal of Physics D: Applied Physics* 45:11, 2012, p. 113001.

[33] J. Homola, S. S. Yee, and G. Gauglitz. "Surface Plasmon Resonance Sensors". *Sensors and Actuators B: Chemical* 54:1-2, 1999, pp. 3–15.

[34] M. Specht, J. Pedarnig, W. Heckl, and T. Hänsch. "Scanning Plasmon Near-Field Microscope". *Physical review letters* 68:4, 1992, p. 476.

[35] P. Berini and I. De Leon. "Surface Plasmon–Polariton Amplifiers and lasers". *Nature photonics* 6:1, 2012, p. 16.

[36] S. A. Maier. *Plasmonics: Fundamentals and Applications.* Springer Science & Business Media, 2007.

[37] F. Wooten. *Optical Properties of Solids.* Academic press, 2013.

[38] S. Kasap and P. Capper. *Springer Handbook of Rlectronic and Photonic Materials.* Springer, 2017.

[39] W. Sellmeier. “Zur Erkarung Der Abnormen Farbenfolge im Spectrum Einiger. Substanzen”. *Annalen der Physik und Chemie* 219, 1871, pp. 272–282.

[40] C. Kittel, P. McEuen, and P. McEuen. *Introduction to Solid State Physics.* Vol. 8. Wiley New York, 1996.

[41] T. V. Shahbazyan and M. I. Stockman. *Plasmonics: Theory and Applications.* Springer, 2013.

[42] A. D. Rakić, A. B. Djurišić, J. M. Elazar, and M. L. Majewski. “Optical Properties of Metallic Films for Vertical-Cavity Optoelectronic Devices”. *Applied optics* 37:22, 1998, pp. 5271–5283.

[43] J. Dionne, L. Sweatlock, H. Atwater, and A. Polman. “Planar Metal Plasmon Waveguides: Frequency-Dependent Dispersion, Propagation, Localization, and Loss Beyond the Free Electron Model”. *Physical Review B* 72:7, 2005, p. 075405.

[44] B. E. Sernelius. *Surface Modes in Physics.* John Wiley & Sons, 2011.

[45] P. B. Johnson and R.-W. Christy. “Optical Constants of the Noble Metals”. *Physical review B* 6:12, 1972, p. 4370.

[46] M. A. García. “Surface Plasmons in Metallic Nanoparticles: Fundamentals and Applications”. *Journal of Physics D: Applied Physics* 44:28, 2011, p. 283001.

[47] B. E. Saleh and M. C. Teich. *Fundamentals of Photonics.* John Wiley & Sons, 2019.

[48] A. W. Snyder and J. Love. *Optical Waveguide Theory.* Springer Science & Business Media, 2012.

[49] A. Karabchevsky, J. S. Wilkinson, and M. N. Zervas. “Transmittance and Surface Intensity in 3D Composite Plasmonic Waveguides”. *Optics express* 23:11, 2015, pp. 14407–14423.

[50] L. Rayleigh. “XXXI. Investigations in Optics, with Special Eeference to the Spectroscope”. *The London, Edinburgh, and Dublin Philosophical Magazine and Journal of Science* 8:49, 1879, pp. 261–274.

[51] D. B. Murphy. *Fundamentals of Light Microscopy and Electronic Imaging*. John Wiley & Sons, 2002.

[52] R. Gilmozzi. “Giant Telescopes of the Future”. *Scientific American* 294:5, 2006, pp. 64–71.

[53] M. I. Stockman. “Nanoplasmonics: Past, Present, and Glimpse into Future”. *Optics express* 19:22, 2011, pp. 22029–22106.

[54] T. Rylander, P. Ingelström, and A. Bondeson. *Computational Electromagnetics*. Springer Science & Business Media, 2012.

[55] K. Yee. “Numerical Solution of Initial Boundary Value Problems Involving Maxwell’s Equations in Isotropic Media”. *IEEE Transactions on antennas and propagation* 14:3, 1966, pp. 302–307.

[56] Lumerical, Inc. *Lumerical FDTD*. URL: https://www.lumerical.com/products/fdtd/.

[57] COMSOL, Inc. *COMSOL Multiphysics*. URL: https://www.comsol.com/.

[58] C. Sheppard. “Approximate Calculation of the Reflection Coefficient From a Stratified Medium”. *Pure and Applied Optics: Journal of the European Optical Society Part A* 4:5, 1995, p. 665.

[59] S. K. Turitsyn, S. A. Babin, A. E. El-Taher, P. Harper, D. V. Churkin, S. I. Kablukov, J. D. Ania-Castañón, V. Karalekas, and E. V. Podivilov. “Random Distributed Feedback Fibre Laser”. *Nature Photonics* 4:4, 2010, p. 231.

[60] A. Korpel. *Acousto-Optics*. Vol. 57. CRC Press, 1996.

[61] A. Yariv et al. *Optical Electronics in Modern Communications*. Vol. 1. Oxford University Press, USA, 1997.

[62] F. Bretherton. “Propagation in slowly varying waveguides”. *Proceedings of the Royal Society of London. Series A. Mathematical and Physical Sciences* 302:1471, 1968, pp. 555–576.

[63] F. Capolino. *Theory and Phenomena of Metamaterials*. CRC press, 2017.

[64] J.-Y. Ou, E. Plum, L. Jiang, and N. I. Zheludev. “Reconfigurable Photonic Metamaterials”. *Nano letters* 11:5, 2011, pp. 2142–2144.

[65] N. I. Landy, S. Sajuyigbe, J. J. Mock, D. R. Smith, and W. J. Padilla. "Perfect Metamaterial Absorber". *Physical review letters* 100:20, 2008, p. 207402.

[66] D. L. Markovich, A. Andryieuski, M. Zalkovskij, R. Malureanu, and A. V. Lavrinenko. "Metamaterial Polarization Converter Analysis: Limits of Performance". *Applied Physics B* 112:2, 2013, pp. 143–152.

[67] A. Pors, M. G. Nielsen, R. L. Eriksen, and S. I. Bozhevolnyi. "Broadband Focusing Flat mirrors Based on Plasmonic Gradient Metasurfaces". *Nano letters* 13:2, 2013, pp. 829–834.

[68] X. Ni, A. V. Kildishev, and V. M. Shalaev. "Metasurface Holograms for Visible Light". *Nature communications* 4, 2013, p. 2807.

[69] J. Valentine, J. Li, T. Zentgraf, G. Bartal, and X. Zhang. "An Optical Cloak Made of Dielectrics". *Nature materials* 8:7, 2009, p. 568.

[70] J. Li and J. B. Pendry. "Hiding Under the Carpet: A New Strategy For Cloaking". *Physical review letters* 101:20, 2008, p. 203901.

[71] H. Chen, C. T. Chan, and P. Sheng. "Transformation Optics and Metamaterials". *Nature materials* 9:5, 2010, p. 387.

[72] B. Walther, C. Helgert, C. Rockstuhl, F. Setzpfandt, F. Eilenberger, E.-B. Kley, F. Lederer, A. Tünnermann, and T. Pertsch. "Spatial and Spectral Light Shaping with Metamaterials". *Advanced Materials* 24:47, 2012, pp. 6300–6304.

[73] S. Steinberg. *Fundamentals of Grid Generation.* CRC press, 1993.

[74] J. P. Turpin, A. T. Massoud, Z. H. Jiang, P. L. Werner, and D. H. Werner. "Conformal Mappings to Achieve Simple Material Parameters for Transformation Optics Devices". *Optics Express* 18:1, 2010, pp. 244–252.

[75] Q. Wu, J. P. Turpin, and D. H. Werner. "Integrated Photonic Systems Based on Transformation Optics Enabled Gradient Index Devices". *Light: Science & Applications* 1:11, 2012, e38.

[76] T. C. Choy. *Effective Medium Theory: Principles and Applications.* Vol. 165. Oxford University Press, 2015.

[77] E. D. Palik. *Handbook of Optical Constants of Solids.* Vol. 3. Academic press, 1998.

[78] H. R. Philipp. "Optical properties of silicon nitride". *Journal of the Electrochemical Society* 120:2, 1973, pp. 295–300.

[79] J. F. Thompson, B. K. Soni, and N. P. Weatherill. *Handbook of Grid Generation.* CRC press, 1998.

[80] T. Zentgraf, Y. Liu, M. H. Mikkelsen, J. Valentine, and X. Zhang. "Plasmonic Luneburg and Eaton Lenses". *Nature nanotechnology* 6:3, 2011, p. 151.

[81] Y. Liu, T. Zentgraf, G. Bartal, and X. Zhang. "Transformational Plasmon Optics". *Nano letters* 10:6, 2010, pp. 1991–1997.

[82] D. Castelló-Lurbe, E. Silvestre, et al. "Inverse Dispersion Engineering in Silicon Waveguides". *JOSA B* 31:8, 2014, pp. 1829–1835.

[83] Y. Shen, N. C. Harris, S. Skirlo, M. Prabhu, T. Baehr-Jones, M. Hochberg, X. Sun, S. Zhao, H. Larochelle, D. Englund, et al. "Deep Learning with Coherent Nanophotonic Circuits". *Nature Photonics* 11:7, 2017, p. 441.

[84] A. Katiyi and A. Karabchevsky. "Figure of Merit of All-Dielectric Waveguide Structures for Absorption Overtone Spectroscopy". *Journal of Lightwave Technology* 35:14, 2017, pp. 2902–2908.

[85] A. Karabchevsky and A. Kavokin. "Giant Absorption of Light by Molecular Vibrations on a Chip". *Scientific reports* 6, 2016, p. 21201.

[86] L.-W. Luo, N. Ophir, C. P. Chen, L. H. Gabrielli, C. B. Poitras, K. Bergmen, and M. Lipson. "WDM-Compatible Mode-Division Multiplexing on a Silicon Chip". *Nature communications* 5, 2014, p. 3069.

[87] B. Stern, X. Zhu, C. P. Chen, L. D. Tzuang, J. Cardenas, K. Bergman, and M. Lipson. "On-Chip Mode-Division Multiplexing Switch". *Optica* 2:6, 2015, pp. 530–535.

[88] I. A. Young, E. Mohammed, J. T. Liao, A. M. Kern, S. Palermo, B. A. Block, M. R. Reshotko, and P. L. Chang. "Optical I/O Technology for Tera-Scale Computing". *IEEE Journal of solid-state circuits* 45:1, 2009, pp. 235–248.

[89] C. Sun, M. T. Wade, Y. Lee, J. S. Orcutt, L. Alloatti, M. S. Georgas, A. S. Waterman, J. M. Shainline, R. R. Avizienis, S. Lin, et al. "Single-Chip Microprocessor that Communicates Directly Using Light". *Nature* 528:7583, 2015, p. 534.

[90] J. Knight, T. Birks, P. S. J. Russell, and J. De Sandro. "Properties of Photonic Crystal Fiber and the Effective Index Model". *JOSA A* 15:3, 1998, pp. 748–752.

[91] M. Yamada, Y. Ohmori, K. Takada, and M. Kobayashi. "Evaluation of Antireflection Coatings for Optical Waveguides". *Applied optics* 30:6, 1991, pp. 682–688.

[92] T. G. Nguyen and A. Mitchell. "Analysis of Optical Waveguides with Multilayer Dielectric Coatings Using Plane Wave Expansion". *Journal of lightwave technology* 24:1, 2006, p. 635.

A Publications

A.1 Journal Publications

1. **Greenberg, Y.** and A. Karabchevsky. "Spatial eigenmodes conversion with metasurfaces engraved on silicon ridge waveguides." Applied Optics 58.22 (2019).

2. P.D. Terekhov, K.V. Baryshnikova, **Galutin, Y.** et al., "Enhanced absorption in all-dielectric metasurfaces due to magnetic dipole excitation." Scientific Reports 9.1 (2019): 3438.

3. **Galutin, Y.**, E. Falek, and A. Karabchevsky. "Invisibility Cloaking Scheme by Evanescent Fields Distortion on Composite Plasmonic Waveguides with Si Nano-Spacer." Scientific Reports 7.1 (2017): 12076.
   In the top 100 Scientific Reports physics papers in 2017.

A.2 Conference Contributions

Proceedings

1. **Galutin, Y.**, E. Falek, and A. Karabchevsky. "Invisibility cloak scheme with composite plasmonic waveguides and metsurface overlayers." Progress In Electromagnetics Research Symposium-Spring (PIERS), 2017.

Others

1. **Greenberg, Y.**, Karabchevsky, A., "Silicon Waveguide Mode Converter Based on Tilted Dielectric Metasurface", OASIS7, Tel-Aviv, Israel, 2019. *Poster.*

2. **Galutin, Y.**, Karabchevsky, A., "Controlling Light in a Metasurface-Perturbed Dielectric Waveguide", NANOIL, Jerusalem, Israel, 2018. *Poster.*

3. Karabchevsky, A., **Galutin, Y.**, "Anti-Reflective All-Dielectric Metasurfaces Engraved on an Optical Waveguide Facet", META Conference, Marseille, France, 2018. *Talk.*

4. **Galutin, Y.**, Falek, E., Karabchevsky, A., "Study of evanescent fields distortion perturbed by nanoparticle with metasurfaces on ridge waveguides", OASIS6, Tel-Aviv, Israel, 2017. *Poster.*

תקציר

ההתנהגות המאקרוסקופית של חומרים תחת השפעת שדה אלקטרומגנטי נקבעת על ידי תכונותיהם המיקרוסקופיות, הנובעות מתוך המבנה האטומי. באנלוגיה לאטומים של חומרים המצויים בטבע, תכונותיהם של מטא-חומרים נובעים מתוך מבנים בקנה מידה קטן יותר מאורך הגל. חומרים אלו מאפשרים שליטה חסרת תקדים על גלים אלקטרומגנטיים יחסית לשימוש בחומרים קונבנציונליים, ובעלי יישומים אלקטרומגנטיים רבים בתחומי המיקרוגלים והאופטיקה, ובמיוחד להתקני גלים מולכים.

בעבודה זו, אנו חוקרים כיצד ניתן להשתמש במטא-חומרים על מנת לשפר את הביצועים של התקנים אופטיים משולבים ולהגדיל את הפונקציות שלהם. אנו עושים שימוש בטרספורמציות אופטיות על מנת להדגים הסתרת אובייקט הנמצא על גבי מוליך גל. בהתקן זה, אנו שולטים בשדות האלקטרומגנטיים המתפשטים במוליך הגל כך שאור הפוגע באובייקט הממוקם עליו אינו מפוזר וכתוצאה מכך הוא בלתי נראה לגל הפוגע.

אנו בוחנים את האופי הבדיד של האופנים במוליכי גל דיאלקטריים ומטמיעים בהם מטא-משטחים המתוכננים בעזרת תיאורית התווך האפקטיבי ליצירת התקני המרת אופנים פשוטים וקומפקטיים בעלי יעילות של מעל ל- 90%. ההמרה נעשית באמצעות מטא-משטחים דיאלקטריים החקוקים בשכבת ההולכה העשויה מסיליקון. טכניקת ההמרה המוצעת ניתנת למימוש המרות אופנים שרירותיות.

אנו מפתחים חיישן תהודה המבוסס על פלזמון משטחי בעל שיפור רגישות של 50% בהשוואה לתצורה הנפוצה באמצעות אופטימיזציה של שכבות דקות במבנה רב שכבתי. אנו מבצעים במקביל חקירה ספקטראלית וזוויתית על מנת לאפיין את ביצועי החיישן.

אנו מדגימים כי ניתן לצמצם הפסדי צימוד בין סיבים אופטיים למוליכי גל מסיליקון על ידי מבנים חרוטיים קטנים יותר מאורך הגל ולקבל העברה של מעל 98%. אנו מחשבים את המבנה האופטימאלי על ידי סימולציות נומריות נרחבות.

עבור כל פרויקט אנו מציגים את מושגי היסוד ואת הניתוחים הנדרשים להבנת התפשטות האור במבנים אופטיים בתת-אורך גל. הפיתוחים התאורטיים, התצפיות המספריות, ותוצאות הניסויים מסוכמים ומנותחים בתזה זו.

אוניברסיטת בן גוריון
הפקולטה למדעי הנדסה
בית הספר להנדסת חשמל ומחשבים
היחידה להנדסת אלקטרואופטיקה ופוטוניקה

פוטוניקה משולבת בתת-אורך גל

מאת

יעקב גרינברג

חיבור זה מהווה חלק מהדרישות לקבלת תואר מגיסטר בהנדסה

בהנחיית

ד"ר אלינה קרבצ'בסקי

יעקב גרינברג	07/01/2020
חתימת הסטודנט	תאריך
Karabchevsky	08/01/2020
חתימת המנחה	תאריך
	8-1-2020
חתימת יו"ר הוועדה המחלקתית	תאריך

ספטמבר 2019

אוניברסיטת בן גוריון
הפקולטה למדעי הנדסה
בית הספר להנדסת חשמל ומחשבים
היחידה להנדסת אלקטרואופטיקה ופוטוניקה

פוטוניקה משולבת בתת-אורך גל

מאת
יעקב גרינברג

חיבור זה מהווה חלק מהדרישות לקבלת תואר מגיסטר בהנדסה

בהנחיית
ד"ר אלינה קרבצ'בסקי

ספטמבר 2019